Draft version August 8, 2018
Preprint typeset using LaTeX style emulateapj v. 03/07/07

EXTENDED SCHMIDT LAW: ROLE OF EXISTING STARS IN CURRENT STAR FORMATION

Yong Shi[1], George Helou[1], Lin Yan[1], Lee Armus[1], Yanling Wu[1], Casey Papovich[2], Sabrina Stierwalt[1]

Draft version August 8, 2018

ABSTRACT

We propose an "extended Schmidt law" with explicit dependence of the star formation efficiency (SFE=SFR/$M_{\rm gas}$) on the stellar mass surface density ($\Sigma_{\rm star}$). This relation has a power-law index of 0.48±0.04 and an 1-σ observed scatter on the SFE of 0.4 dex, which holds over 5 orders of magnitude in the stellar density for individual global galaxies including various types especially the low-surface-brightness (LSB) galaxies that deviate significantly from the Kennicutt-Schmidt law. When applying it to regions at sub-kpc resolution of a sample of 12 spiral galaxies, the extended Schmidt law not only holds for LSB regions but also shows significantly smaller scatters both within and across galaxies compared to the Kennicutt-Schmidt law. We argue that this new relation points to the role of existing stars in regulating the SFE, thus encoding better the star formation physics. Comparison with physical models of star formation recipes shows that the extended Schmidt law can be reproduced by some models including gas free-fall in a stellar-gravitational potential and pressure-supported star formation. By implementing this new law into the analytic model of gas accretion in Λ CDM, we show that it can re-produce the observed main sequence of star-forming galaxies (a relation between the SFR and stellar mass) from z=0 up to z=2.

Subject headings: galaxies: evolution – galaxies: starburst – stars: formation – ISM: molecules – ISM: HI

1. INTRODUCTION

Stars form from the cold interstellar medium (ISM). The resulting stellar mass growth, chemical enrichment and energy feedback to the ISM and intergalactic medium (IGM) are key processes of galaxy formation and evolution. Understanding how stars form is thus one of the central questions in galactic and extragalactic astronomy. Star formation invokes a series of complicated processes from gas accretion, gas cooling and H_2 formation to the final molecular cloud collapse and stellar feedback. Empirical scaling laws between star formation and gas reservoirs provide critical tests of our modeling of the above various processes and have crucial applications to studies of galaxy formation and evolution in the cosmological context.

In the pioneering work of Schmidt (1959), a simple power law relation is proposed to relate the star formation rate (SFR) density to the gas density:

$$\rho_{\rm SFR} = A\rho_{\rm gas}^{N_{\rm SFR}} \quad (1)$$

where $\rho_{\rm SFR}$ is the SFR volume density, $\rho_{\rm gas}$ is the volume density of total cold gas including HI and molecular hydrogen (H_2) and $N_{\rm SFR}$ is the power index while A is simply assumed to be constant. Kennicutt (1989, 1998a) demonstrated this unambiguously in its observable form (surface density) with 61 nearby spiral galaxies and 36 infrared-selected nuclear starburst regions that span a large dynamic range and concluded:

$$\Sigma_{\rm SFR} \propto \Sigma_{\rm gas}^{1.4\pm0.15} \quad (2)$$

which is often referred as the Kennicutt-Schmidt (KS) law. It makes general sense that the gas reservoir determines how many stars can form, i.e., the gas density plays the dominant role in regulating SFR. With this basic relation between SFR and gas, the star formation efficiency (SFE=SFR/gas-mass in this study) follows:

$$\mathrm{SFE} = \frac{\Sigma_{\rm SFR}}{\Sigma_{\rm gas}} \propto \Sigma_{\rm gas}^{N_{\rm SFE}}, \text{ with } N_{\rm SFE} = 0.4 \quad (3)$$

It should be noted that the KS law does not hold for the whole range of gas densities. An accompanying rule is the star formation threshold, introduced to explain the fact that the SFR is significantly lower than predicted by the KS law at low gas densities (<∼1-10 $M_\odot$ pc^{-2}), e.g., in low-surface-brightness (LSB) galaxies or regions far outside the optical disk (e.g. Martin & Kennicutt 2001; Wyder et al. 2009; Bigiel et al. 2008; Roychowdhury et al. 2009). Other forms of the Schmidt law [3] have also been proposed, such as those that invoke the dynamical factors (Silk 1997; Elmegreen 1997; Boissier et al. 2003):

$$\mathrm{SFE} \propto \frac{1}{\tau_{\rm dyn}} \quad (4)$$

where $\tau_{\rm dyn}$ is the orbital dynamical timescale. This relation has been demonstrated to predict the SFR as well as the KS law when considering the orbital timescale (Kennicutt 1998a), while the break may still show up at the low density end (Wyder et al. 2009).

Although the above two Schmidt relations are valid for a range of galaxy types both in the local universe (e.g. Kennicutt 1998a; Bigiel et al. 2008) and at high-z (e.g. Daddi et al. 2010b; Genzel et al. 2010), it is surprising that they only invoke the gas component while in reality various ISM and stellar components are intimately involved in processes of converting gas into new stars.

[1] Infrared Processing and Analysis Center, California Institute of Technology, 1200 E. California Blvd, Pasadena, CA 91125
[2] George P. and Cynthia Woods Mitchell Institute for Fundamental Physics and Astronomy, Department of Physics and Astronomy, Texas A&M University, College Station, TX 77843-4242

[3] In this study we expand the definition of the Schmidt law to include any relationship that invokes SFRs and gas, which shares the initial idea that Schmidt proposed.

Many of these processes are related to existing stars that form over the whole galaxy's history. For example, the gravitational effects of stellar bars can remove gas angular momentum and increase nuclear SFRs in normal galaxies (e.g. Sérsic & Pastoriza 1967; Ho et al. 1997). Their effects are also recognized in numerical simulations of gas-rich galaxy merging and thought to be the main factor to determine how much gas can be converted into stars (Hopkins et al. 2009a,b). The gas hydrostatic pressure produced by gas self-gravity and stellar gravity is further shown empirically to be related to the H_2-to-HI ratio (Elmegreen & Parravano 1994; Wong & Blitz 2002; Blitz & Rosolowsky 2004, 2006). Besides the stellar gravity, the metal outputs of stellar evolution are the main coolants of gas and thus star formation should show dependencies on the metallicity. Theoretical works have indicated significantly lower SFEs at low metallicity (Krumholz et al. 2009; Gnedin & Kravtsov 2010). Dust grains that form from metals catalyze the H_2 formation and shield it from radiation destruction (for a review, see Hollenbach & Tielens 1999). Current proposed Schmidt relations do not have any hint for these effects, as they only invoke the gas component.

To evaluate the importance of existing stars in the empirical scaling law, we demonstrate the existence of a tight relationship between SFEs and stellar mass surface densities, referred as the extended Schmidt law. This relation not only predicts the SFE and SFR as well as the KS law for galaxies and spatially-resolved regions ($\sim$1 Kpc sizes) where the KS law works, but also holds for LSB galaxies and regions where the KS law fails. Similar close links between star formation and total stars have been recognized in previous works for certain galaxy types or limited stellar mass surface density ranges. For example, Hunter et al. (1998) have shown for radial azimuthally-averaged quantities in LSB galaxies that the stellar mass density is the only quantity spatially related to the SFR density. Similar close associations between stellar masses and SFR densities are also seen within and among galaxies by Ryder & Dopita (1994), Brosch et al. (1998), Hunter & Elmegreen (2004) and recently by Leroy et al. (2008) for specific galaxy types or limited density ranges. Here, we demonstrate this intimate association directly by showing a tight relation between the SFE and stellar mass density over a large dynamic range. In § 2, we present the sample selection and data collection. We show the result in § 3. In § 4, we first compare the extended Schmidt law to the model of the star formation recipe and then discuss its implication for the main sequence of star-forming galaxies. Conclusions are presented in § 5. Throughout this paper, we assume H_0=70 km s^{-1} Mpc^{-1}, Ω_0=0.3 and Ω_Λ=0.7.

2. SAMPLE AND DATA

2.1. *Individual Global Galaxies*

Our whole sample is listed in Table 1 and composed of five sub-samples including low-redshift late-type galaxies, early-type galaxies, LSB galaxies, luminous infrared galaxies and high-z objects. The CO and HI data are collected from the literature. Molecular gas masses are derived from the CO by assuming a constant CO-to-H_2 conversion factor of $X_{\rm CO}$=2.0$\times$10^{20} cm^{-2} (K km s^{-1})$^{-1}$ or 3.17 M$_\odot$ pc^{-2} (K km s^{-1})$^{-1}$ or 7845$d_{\rm L}^2$ M$_\odot$ (Jy km s^{-1})$^{-1}$ where $d_{\rm L}$ is the luminosity distance in Mpc (Dickman et al. 1986; Solomon et al. 1987; Tacconi et al. 2008). Different conversion factors for mergers and non-mergers are also discussed in § 3.1. A factor of 1.36 is further included to account for the presence of heavier elements in both the H_2 and HI masses. The SFR data are collected from the same references as the gas data (see Table 1), and all are corrected to Chabrier initial mass function (IMF) where SFR$_{\rm Chabrier}\approx$SFR$_{\rm Kroupa}$=0.66SFR$_{\rm Salpeter}$ (Bruzual & Charlot 2003).

The stellar masses are measured by fitting the Bruzual & Charlot (2003) population synthesis model to the multi-band SED with Chabrier IMF following Shi et al. (2008). The details of the parameters to produce the models are listed in Table 2. The model of Bruzual & Charlot (2003) generally produces consistent color and mass-to-light ratio at various bands compared to others (Vázquez & Leitherer 2005). However, it still lacks accurate evolutionary tracks of thermally pulsing asymptotic giant branch (AGB) stars. At the stellar age around 0.1-3 Gyr where AGB stars are prominent, the mass-to-light ratio in the near-IR can be overestimated by $\sim$60% (Maraston et al. 2006; Bruzual 2007). The effect of this on the result of this paper is shown to be small (see § 3.1). To minimize systematic errors that may be caused by different template population models, the range of input parameter spaces, numerical method and etc, we have applied the above method to all of our objects except for 23 galaxies from Leroy et al. (2008) whose masses are derived from IRAC 3.6 μm emission in that work. For these objects, the published gas and SFR surface densities are defined within $1.5R_{25}$ where the available optical photometry does not exist. For the spiral objects in their sample where the majority (>95%) of the optical light is enclosed within R_{25} (Courteau 1996), the median offset between their stellar masses and ours by fitting models to optical/IRAC photometry is only 0.1 dex. The broad-band wavelengths used to calculate the stellar masses for all objects are listed in Table 1 and the majority covers both the optical and near-IR bands.

The surface densities of gas, SFR and stellar masses are measured within the same aperture and corrected for inclinations. Table 1 lists the aperture definitions and their relations to optical isophotal radii (R_{25}) if available in Paturel et al. (2003)[4]. Different apertures are adopted for different galaxy types, partly because of the heterogeneous nature of the sample but also because of different light structures of individual galaxy types. Since a star formation law describes how star forms from gas, an ideal aperture for a galaxy-averaged star formation relationship should enclose the majority of star formation or gas. This certainly results in different aperture sizes for galaxies with different types, e.g., compact apertures for ultra luminous infrared galaxies (ULIRGs) and wide ones for low surface-brightness (LSB) galaxies. As discussed in § 3.1, the extended Schmidt law depends little on how exactly an aperture is defined. We estimated a typical error of 0.30 dex for each quantity (SFR, gas and stellar mass densities) based on our own experiences of measurements, while local LIRGs and high-z galaxies have higher uncertainties ($\sim$0.5 dex) due to low spatial

[4] http://leda.univ-lyon1.fr/

resolution.

1. Late-type galaxies: This subsample includes 61 and 18 objects from Kennicutt (1998a) and Leroy et al. (2008), respectively. For 11 objects included in both samples, the data from the latter is used in this work because of higher data quality. Galaxies from Kennicutt (1998a) have published SFR and gas surface densities that are defined to be within the optical isophotal radii (R_{25}, de Vaucouleurs et al. 1976). The SFR is based on the extinction-corrected Hα emission with $A_{H\alpha}$=1.1 mag (see their paper for the equation). The optical/near-IR photometry used to derive stellar masses are collected from NED. Since the aperture of R_{25} encloses the majority (>95%) of optical light for spiral galaxies (Courteau 1996), the aperture-matched stellar mass density is thus defined by dividing the total mass with πR_{25}^2. All spiral galaxies from Leroy et al. (2008) have published gas, SFR and stellar mass densities, where the aperture radius is defined to be $1.5r_{25}$. The SFR is measured from the combination of FUV and 24 μm emission (see their paper for the equation). For 11 objects from this study also included in the sample of Kennicutt (1998a), we checked the median offset in the stellar mass between ours and theirs is only 0.1 dex.

2. Early-type galaxies: Low level star formation has been detected in circumnuclear regions of many early-type galaxies (Shapiro et al. 2010; Wei et al. 2010; Crocker et al. 2011). Although the difficulty of SFR measurements due to contamination from large populations of old stars and possible AGN, these objects are shown to follow more or less the Kennicutt-Schmidt law. We here included nine objects from Wei et al. (2010) and 10 objects from Crocker et al. (2011). Wei et al. (2010) have published aperture-matched H_2 mass from CO data and SFR from a combination of 24 μm and UV emission following Leroy et al. (2008). For six of nine objects, we estimated the HI mass from the available VLA HI map in the literature (see Table 1) and found that the HI mass in the CO-aperture is < 10% of the total HI. Based on this, we therefore included three more objects with the total HI mass < 1.6 times the H_2 mass, which implies the HI mass within the CO aperture is smaller than 16% of H_2. Objects in Crocker et al. (2011) have available aperture-matched total gas mass and SFR measurements. As recommended in that work, we have used 24μm+Hα or PAH+Hα if available and radio+Hα for two more objects, where they have used formula calibrated in Kennicutt et al. (2009) (see their Table 4). For objects from both works, the aperture-matched stellar mass density is estimated in this work by fitting the stellar synthesis models to the aperture-matched 2MASS J, H and K photometry and SDSS optical photometry for most of them.

3. Low-surface-brightness (LSB) galaxies: We defined the LSB objects as an independent subsample as they show deviations from the KS law. The subsample includes all the 19 objects from Wyder et al. (2009) and 5 gas-rich dwarf galaxies from Leroy et al. (2008) that have stellar mass surface densities below 1 $M_\odot$ pc^{-2} that is roughly the upper limit of the Wyder et al. (2009) sample. Wyder et al. (2009) measured the surface densities of the SFR and gas mass through UV emission (using Kennicutt (1998b) equation) and HI, respectively, where the aperture is defined to be the minimum of the maximum radii of UV and HI emission. For these objects, the contribution from obscured star formation should be negligible to the total SFR (e.g. Hinz et al. 2007), while the HI should dominate the total gas mass (e.g. Matthews et al. 2005; Leroy et al. 2008). We derived the stellar mass from the SDSS photometry while additional near-IR photometry from NED was also used for two objects. As the published SDSS data under-estimate the sizes and thus brightness of these objects, we have remeasured five-band SDSS photometry in the aperture adopted in Wyder et al. (2009). The majority of these objects have optical emission out to the adopted radius as observed by SDSS (see the r-band radial profile in Wyder et al. (2009)). The comparison of our r-band photometry to those measured by Wyder et al. (2009) shows <10% discrepancy. All dwarf galaxies from Leroy et al. (2008) have published gas, SFR and stellar mass densities within $1.5r_{25}$.

4. Local LIRGs (z=0 LIRGs): We have collected seven local LIRGs from the literature with two criteria: (1) the spatially-resolved CO interferometer images are available and well resolved (i.e. the deconvolved size is larger than the resolution); (2) the interferometer fluxes recover the majority (>90%) of single-dish measurements. As listed in Table 1, the aperture to define the surface density is the maximum extent of the CO emission. For the total gas density, we have neglected the contribution from the atomic gas in these gas rich objects. Since star formation takes place in molecular clouds, we assume all star formation is included in the CO aperture where the SFR is based on the IR luminosity assuming Kennicutt (1998b) relations and corrected to Chabrier IMF. To measure the aperture-matched stellar mass density, we first calculated the total mass by fitting stellar models to the UV/optical/near-IR SED collected from NED, and then measured the part in the CO aperture with the HST/ACS-F814w image assuming a constant mass-to-light ratio, which can cause additional stellar mass uncertainty (∼0.3 dex).

5. High-redshift star-forming galaxies (high-z SFGs) and merging sub-millimeter galaxies (high-z SMGs): We here included 21 optically/near-IR selected star-forming galaxies (EGS, BzK and BXMD) and 7 sub-millimeter objects from Genzel et al. (2010). The SFR and gas are available in that work. The SFR for the EGS is estimated from a combination of extinction-corrected Hα/[O II]/GALEX-UV and Spitzer 24 μm emission. For the BzK, it is a combination of extinction-corrected UV and 24 μm emission. For the BXMD objects, it is from extinction-corrected Hα emission while the SFR of the SMG is from 850 μm emission (see Genzel et al. (2010) for the equation) . We measured stellar masses by our own to reduce systematic errors among different studies. The median offset of our stellar masses compared to the literature data are -0.16 dex, 0.34 dex, -0.55 dex and 0.00 dex for EGS, BzK, BXMD and submm galaxies, respectively (see Genzel et al. (2010), Daddi et al. (2010), Erb et al. (2006) and Hainline et al. (2010), respectively). The large offsets for BXMD (z ∼2.2) and BzK (z ∼1.5) are mainly due to the lack of the rest-frame near-IR photometry, which could cause large differences when different template SEDs are used. With the unified stellar mass measurement, the scatter among them in the extended Schmidt law does become smaller. The

galaxy size is defined as the half light radius obtained from the fit to Hα, optical/UV or CO images. Similar to Genzel et al. (2010), all densities are defined within the half light radius ($R_{1/2}$), e.g., $\Sigma_{\rm star} = 0.5{\rm M_{star}}/(\pi R_{1/2}^2)$. Here we did not account for the difference in the half-light radius among SFR, gas and stars for individual galaxies, since these three half light radii are on average quite close to each other (e.g. Swinbank et al. 2010).

2.2. *Individual Regions In Spiral Galaxies*

With the advent of high spatial-resolution SFR, gas and stellar images of nearby galaxies, the star formation law at sub-kpc scales have been studied extensively (e.g. Wong & Blitz 2002; Jogee et al. 2005; Crosthwaite & Turner 2007; Schuster et al. 2007; Kennicutt et al. 2007; Bigiel et al. 2008; Leroy et al. 2008). The general conclusion is that the relationship between SFR and total gas varies strongly both within galaxies and across different objects. This implies that the physics other than those directly related to the total gas strongly affect the SFE of the total gas. To test the idea of the SFE regulated by existing stars as proposed by the extended Schmidt law, we have carried measurements of SFR, gas and stellar masses in a sample of 12 spiral galaxies as listed in Table 3. They are derived from The HI Nearby Galaxy Survey (THINGS, Walter et al. 2008) and The SIRTF Nearby Galaxies Survey (SINGS, Kennicutt et al. 2003).

For each object, the SFR and gas mass are measured within individual 750×750 pc^2 regions across the main optical disk (semi-major axis $< R_{25}$), with the technical procedure basically following Bigiel et al. (2008) (also see Leroy et al. 2008) but corrected to our IMF and CO-to-H_2 conversion factors. The SFR is estimated from combination of GALEX far-UV (Gil de Paz et al. 2007) and Spitzer 24 μm (Kennicutt et al. 2003), with the 3-σ lower-limit around 10^{-4} M$_\odot$/yr/kpc^2. The gas mass is derived from a combination of THINGS HI data (Walter et al. 2008) and BIMA SONG CO J=1-0 map (Helfer et al. 2003), with the limiting surface density around 1.5 M$_\odot$ pc^{-2}. Since the spatial coverage of BIMA SONG does not extend significantly beyond the HI-to-H_2 transition radius where the total gas is dominated by HI emission, we have extrapolated the CO data to pixels without observations based on the observed CO/HI ratio as a function of semi-major axis. The result changes little if adopting the mean CO/HI ratio as a function of radius derived from Leroy et al. (2008). For seven galaxies with significantly extended CO coverage in Bigiel et al. (2008), our derived slope of the KS law is consistent with theirs within 20%. The stellar mass is estimated based on the mass-to-light ratio at Spitzer 3.6 μm. The SINGS 3.6 μm image is further subtracted by the median sky level after binning to the resolution of 750×750 pc^2, while the 3-σ sky fluctuation gives the limiting stellar mass surface density around 1 M$_\odot$ pc^{-2}. To reduce the effect of radial gradient of stellar age, extinction and metallicity on the stellar mass measurement, the 3.6μm mass-to-light ratio is derived based on the optical color, for which the theoretical trend is computed from our stellar population synthesis models with solar and 0.25 solar metallicity. For five galaxies with available SDSS images, the optical color is defined to be the g-r color, while the mean trend of these objects is used for the remaining objects.

3. RESULTS

3.1. *The Extended Schmidt Law For Individual Galaxies*

By treating $\Sigma_{\rm SFR}$ as a dependent variable, and $\Sigma_{\rm gas}$ and $\Sigma_{\rm star}$ as independent variables, we search for the best power-law exponents relating them. A linear regression fit (IDL regress.pro) gives:

$$\Sigma_{\rm SFR} \propto \Sigma_{\rm gas}^{1.13\pm0.05}\Sigma_{\rm star}^{0.36\pm0.04} \quad (5)$$

The most important result of the fit is that the derived index for $\Sigma_{\rm star}$ is not zero that would be expected by the KS law. Secondly, the derived exponent for $\Sigma_{\rm gas}$, namely approximately unity, suggests a clear physical implication of the relation, i.e., that the SFE ($=\Sigma_{\rm SFR}/\Sigma_{\rm gas}$) is related to the stellar mass surface density. We thus carry out directly the fit between SFE and $\Sigma_{\rm star}$ as shown in Figure 1(a) through a Bayesian approach to linear regression (Kelly 2007) that also accounts for uncertainties in both variables. As shown in Table 4, the best-fit gives:

$$\frac{\rm SFE}{\rm yr^{-1}} = 10^{-10.28\pm0.08}\left(\frac{\Sigma_{\rm star}}{\rm M_\odot pc^{-2}}\right)^{0.48\pm0.04} \quad (6)$$

where errors of the best-fit parameters are the intrinsic ones. The SFE-$\Sigma_{\rm star}$ relation is obviously different from the KS law, although both of them could be used to predict the SFE. By invoking the stellar mass density, the SFE-$\Sigma_{\rm star}$ correlation describes another scaling relation for star formation with emphasis on the role of the existing stellar component in the current star formation activity. In what follows, we refer to the relation in Equation 6 or the SFE-$\Sigma_{\rm star}$ relation as the extended Schmidt law as it includes additional parameter (stellar surface density).

We now compare the extended Schmidt law to the KS law in the ability to predict the SFE and SFR for various galaxy types as shown in Figure 1 and Figure 2, respectively. The main difference of the extended Schmidt law from the standard KS law is to bring the LSB objects back to the relationship. While the KS law was first defined for late-type galaxies and LIRGs (Kennicutt 1989, 1998a), LSB galaxies/regions show significant deviations from it (e.g. Kennicutt 1998a; Martin & Kennicutt 2001; Bigiel et al. 2008; Wyder et al. 2009; Roychowdhury et al. 2009). The median offsets of the LSB from the best fit are -0.75 dex and -0.71 dex in Figure 1(b) and Figure 2(b), respectively, where the best-fit is done by excluding LSB and early-type objects due to their apparent offsets. The cause for this deviation is still unclear but is most likely related to some instabilities either gravitationally or thermally and chemically. On the other hand, these LSB objects follow more or less the extended Schmidt law with median offsets of -0.16 and -0.08 dex in two figures, respectively, where the fit is done for all objects. This is the main advantage of the extended Schmidt law compared to the KS one. The observed scatter of the extended Schmidt law is slightly smaller than that of the KS law (see Table 4). For early-type galaxies, we here included objects from studies of Wei et al. (2010) and Crocker et al. (2011). They follow more or less the KS law with median offsets of 0.30 dex and 0.32 dex toward higher SFE (Figure 1(b)) and SFR (Figure 2(b)), respectively. The objects from Wei et al. (2010) show slightly larger offsets than Crocker et al. (2011), probably due to

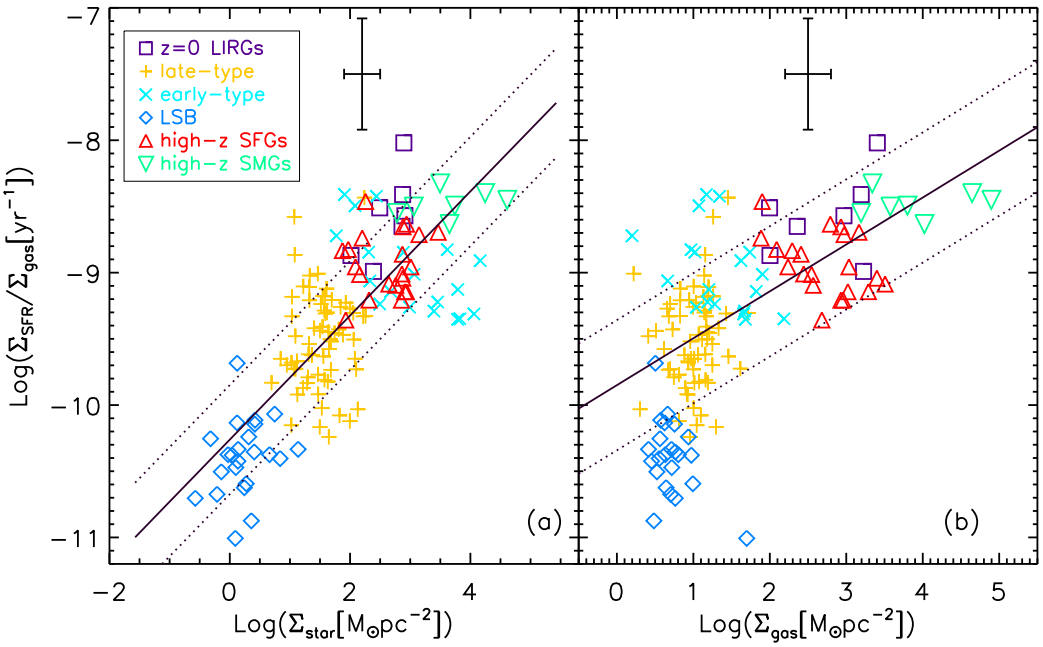

FIG. 1.— **(a):** The star-formation efficiency ($=\Sigma_{\rm SFR}/\Sigma_{\rm gas}$) as a function of the stellar mass surface density. **(b):** The SFE as a function of the gas density. The solid and dotted lines are the intrinsic best-fit and observed 1-σ scatter, respectively, as listed in Table 4. The fit to the SFE-$\Sigma_{\rm gas}$ (right panel) is done excluding LSB and early-type galaxies. Typical error bars are plotted.

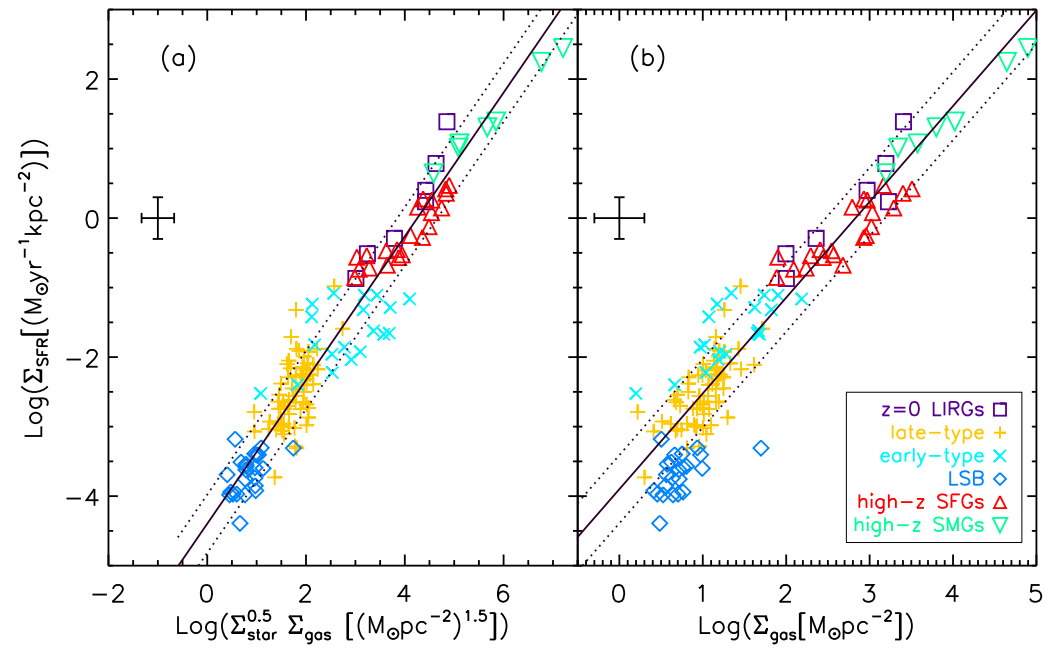

FIG. 2.— Comparison between the extended Schmidt law and Kennicutt-Schmidt relationship in the ability to predict the SFR. The solid and dotted lines are the intrinsic best-fit and observed 1-σ scatter, respectively, as listed in Table 4. The fit to the KS law (right panel) is done excluding LSB and early-type galaxies. Typical error bars are plotted.

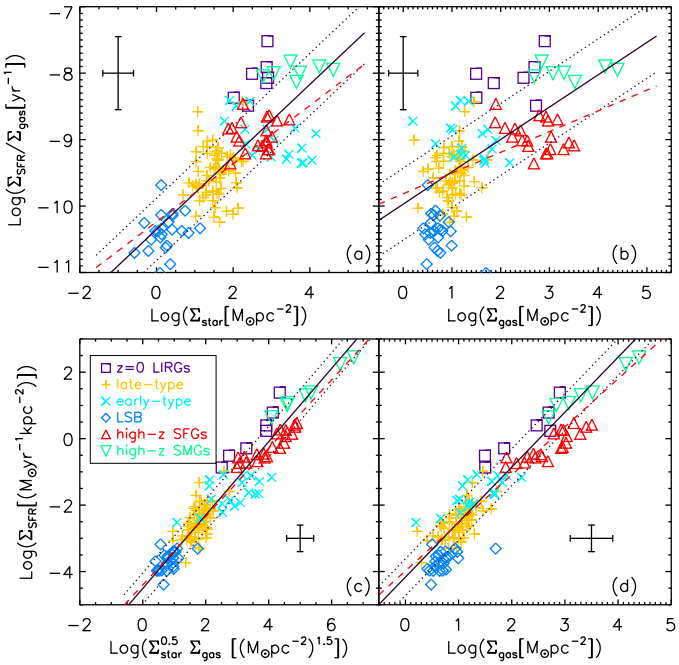

FIG. 3.— Similar to Figure 1 and Figure 2 but using different CO-to-H_2 conversion factors for normal galaxies (α=3.17 $M_\odot$ pc^{-2} (K km s^{-1})$^{-1}$) and merging objects (local LIRGs and high-z submillimeter galaxies; α=1.0 $M_\odot$ pc^{-2} (K km s^{-1})$^{-1}$). The solid and dotted lines are the intrinsic best-fit and observed 1-σ scatter, respectively, to all data points but excluding LSB and early-type galaxies for panel (b) and (d). The dashed lines show the best fit to all the non-mergers but excluding LSB and early-type ones for panel (b) and (d).

the contribution from old stellar populations to the UV emission that has been included in their SFR measurements. As shown in Figure 1(a) and Figure 2(a), these early-type galaxies lie generally on the extended Schmidt law with median offsets of -0.19 dex and -0.26 dex on two figures, respectively. As a summary, we found that the extended Schmidt law is a universal relationship that holds for various galaxy types especially including LSB ones that do not follow the KS law.

As described in § 2.1, different galaxy apertures are used for different galaxy types. As listed in Table 1, their relative sizes to optical isophotal radii R_{25} ranges from around $0.2R_{25}$ for LIRGs and early-type galaxies with circumnuclear star formation to 2-3R_{25} for LSB galaxies with widely-distributed star formation. Most of these apertures are indeed defined to enclose the majority of star formation and gas, which is consistent with the definition of star formation law that empirically describes how stars from gas. In spite of different apertures, the extended Schmidt law depends little on the aperture size as long as three quantities (SFR, gas and stellar mass) are measured within the same aperture which is what has been done in this study. As shown in the below, galaxies basically move along the relation without large offsets from the best-fit if different apertures are used. For 11 LSB galaxies from Wyder et al. (2009) with available radial profiles of SFR, gas and stellar mass, we measured the relative offset in the Y-axis from the best-fit compared to the aperture ($\sim 2R_{25}$) used in Figure 2. Three apertures of $0.2R_{25}$, $0.5R_{25}$ and R_{25} are tested. Although they move along the relation, the median relative offsets are only -0.02 dex, 0.12 dex and 0.04 dex, respectively, where the positive sign mean offset toward higher SFRs. For 12 spiral galaxies with apertures of $1.5R_{25}$ from Leroy et al. (2008), the median offset for $0.5R_{25}$ and R_{25} are -0.1 dex and -0.02 dex, respectively. For early-type and ULIRGs, if we assume no star formation and gas outside the circumnuclear region, the median offset will be around 0.3 dex and 0.6 dex for the aperture radius of 0.5 R_{25} and R_{25}, respectively, which is still with tolerance given the observed 1-σ scatter of 0.5 dex in Figure 2. Overall, we have found that the extended Schmidt law changes a little if the aperture radius vary several times (3-5).

Accurate stellar mass measurements are important to the result of the extended Schmidt law. To reduce systematic errors by different studies, we have measured the masses by our own based on Bruzual & Charlot (2003) model for almost all objects except for 23 galaxies in Leroy et al. (2008) for which the median offset from our method is only 0.1 dex. The Bruzual & Charlot (2003) model underestimates the contribution from AGB stars in the near-IR and thus overestimates the near-IR mass-to-light ratio at ages around 0.1-3Gyr. If the stellar masses are reduced by 60% for galaxies with characteristic ages defined by stellar-mass/SFR around the above range, the slope of the extended Schmidt law increases only by $\sim$0.01 dex. As listed in Table 2, we adopted exponentially declining or constant star formation history (SFH). If the SFH is exponentially increasing for the high-z objects (Maraston et al. 2010; Papovich et al. 2010), the inferred stellar mass decreases by about 0.2 dex and the slope of the extended Schmidt law only increases by 0.01 dex. We notice that the photometric coverage of LSB galaxies is generally not as good as other types. While those from Wyder et al. (2009) is essentially based on the SDSS optical photometry, the ones from Leroy et al. (2008) are based on IRAC 3.6 μm. The median offset in the stellar mass density between the two subsample is only 0.04 dex, implying that there is no significant bias in the mass estimate based only on either optical or near-IR photometry.

Recently Schiminovich et al. (2010) published the HI-based SFE measurement for a large sample of local massive galaxies ($M_* > 10^{10}$ $M_\odot$). They claimed an almost constant SFE ($10^{-9.5}$ yr^{-1}) in their sample for a range of log($\Sigma_{\rm star}$) of 2 to 3.3 $M_\odot$kpc^{-2}. The detailed comparison to our result is hampered by the lack of the H_2 data of their objects, possible large uncertainties in their SFR measurements (UV-based ones vs. our recombination-line/IR/UV based ones) and most importantly the aperture-unmatched SFE measurements relative to those of the stellar densities measured within the half light radius ($r_{1/2}$). To estimate a rough deviation of their sample from the prediction of our relation given their median density, we assume $M_{\rm HI+H_2}/M_{\rm HI} \approx 10$ within $r_{1/2}$ (Leroy et al. 2008) and $M_{\rm HI}^{\rm tot}/M_{\rm HI}^{r_{1/2}} \approx 50$ derived from the THINGS HI radial profile in Walter et al. (2008). The resulting offset is < 0.3 dex.

The above studies assume the same CO-to-H_2 factor (α value) for all galaxies, while this factor is likely to be different in local ULIRGs and high-z merging galaxies from normal galaxies. To quantify the effect of different α values in the relation, we show the relations in Figure 3 with α = 3.17 $M_\odot$ pc^{-2} (K km s^{-1})$^{-1}$

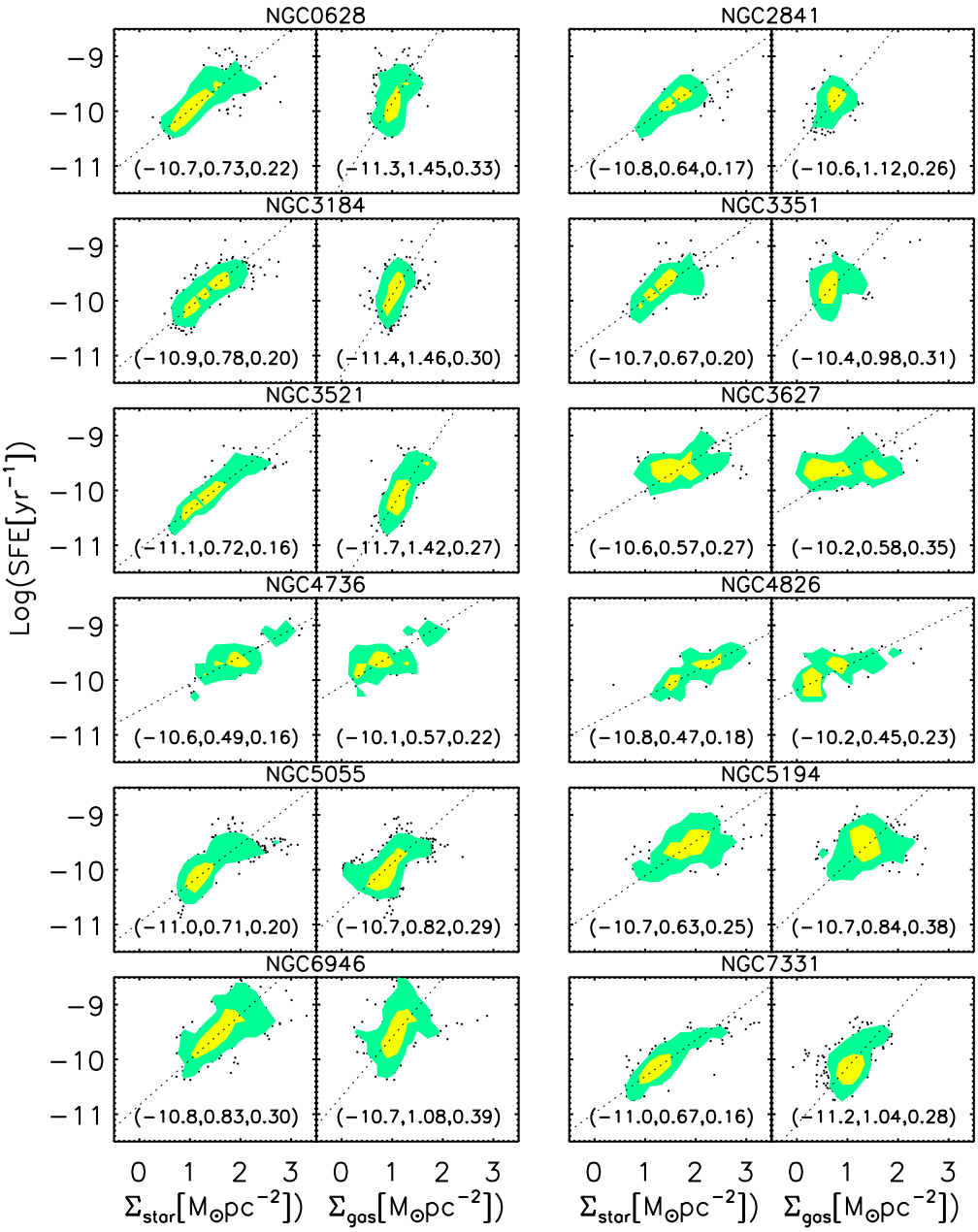

FIG. 4.— The extended Schmidt law at sub-kpc resolution (the left side of each panel) compared to the KS law (the right side of each panel) in a sample of 12 spiral galaxies. The filled yellow and green areas enclose 50% and 90% of the total datapoints, respectively, while the dots are those outside the 90% area. The numbers listed in the parenthesize are in a sequence of interception, slope and 1-σ observed scatter as given by the ordinary least squares bisector fit (Isobe et al. 1990), while the dotted line is the best fit.

for normal galaxies (Dickman et al. 1986; Solomon et al. 1987; Tacconi et al. 2008) and α=1.0 $M_\odot$ pc^{-2} (K km s^{-1})$^{-1}$ for merging galaxies (z=0 LIRGs and high-z sub-millimeter galaxies in this study) (Downes & Solomon 1998; Tacconi et al. 2008). For the KS law (Figure 3(d)), the median offsets of the merging galaxies from the best fit to all data points and non-merging galaxies excluding LSB and early-type ones are 0.48 and 0.81 dex, respectively, which is consistent with the result obtained by Genzel et al. (2010) and Daddi et al. (2010b). For the extended Schmidt law (Figure 3(c)), merging galaxies offsets of 0.58 and 0.74 dex from the best fit to all objects and star-forming galaxies, respectively, which is also comparable to the case of the SFE-$t_{\rm dyn}$ relationships (0.5-0.7 dex by Genzel et al. (2010) and about 0.3 dex by Daddi et al. (2010b)). Thus even in the case of different CO-to-H_2 factors for mergers, the basic idea that the SFE is regulated by the stellar density still holds.

3.2. *The Extended Schmidt Law At Sub-Kpc Resolution*

The result of the extended Schmidt law at sub-kpc resolution in 12 spiral galaxies is shown in the left hand of each panel in Figure 4. It clearly indicates that the SFE is also a function of the stellar mass density for sub-kpc regions in individual spiral galaxies. This demonstrates that the extended Schmidt law proposed for global galaxies in the above section also works at sub-kpc resolution. Compared to the KS law as shown in the right hand of

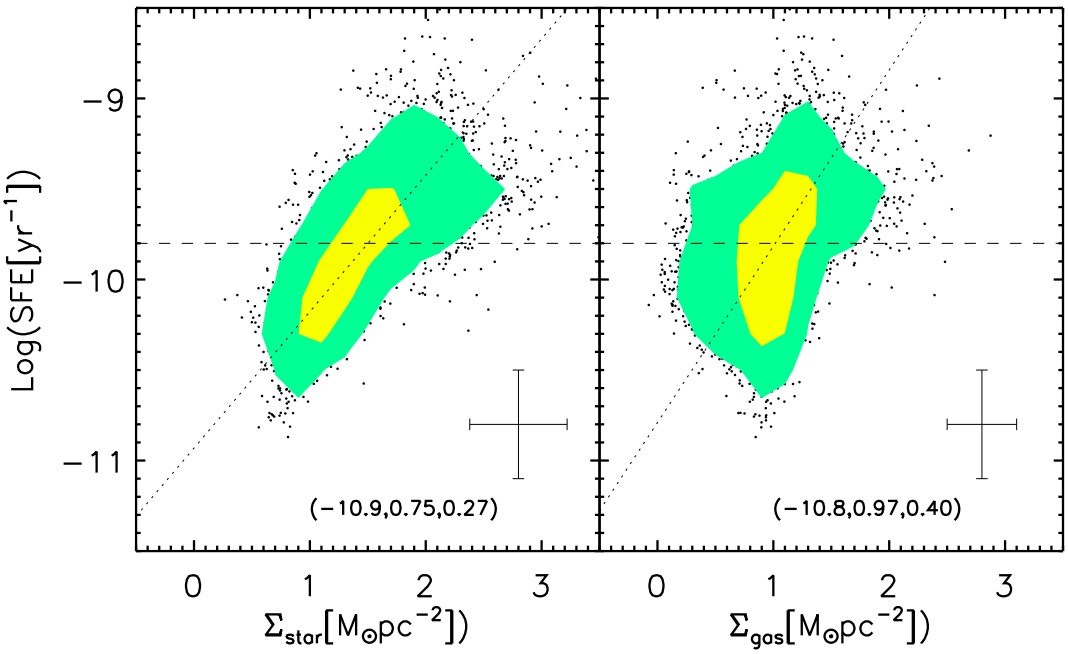

FIG. 5.— The extended Schmidt law at sub-kpc resolution (the left side of each panel) and the KS law (the right side of each panel) of all sub-kpc regions in 12 spiral galaxies. The filled yellow and green areas enclose 50% and 90% of the total datapoints, respectively, while the dots are those outside the 90% area. The numbers listed in the parenthesize are in a sequence of interception, slope and 1-σ observed scatter as given by the ordinary least squares bisector fit (Isobe et al. 1990), while the dotted line is the best fit. The horizontal dashed line marks the transition below which the KS law has a much steeper slope (also see Bigiel et al. 2008).

each panel, the extended Schmidt law shows significantly smaller scatter. Within individual galaxies, the observed scatter of the extended Schmidt law is on average 1.5 times smaller than that of the KS law. Across 12 galaxies, the mean and standard deviation of the slope of the extended Schmidt law is 0.66±0.11 whose scatter is three times smaller than that of the KS law (0.98±0.35).

Figure 5 shows the overall trend for all galaxies. A linear regression fit (IDL regress.pro) to gas mass, stellar mass and SFR surface densities gives:

$$\Sigma_{\rm SFR} \propto \Sigma_{\rm gas}^{0.80\pm0.01}\Sigma_{\rm star}^{0.63\pm0.01} \quad (7)$$

Again, the exponent of the stellar mass density is significantly from zero, indicating the importance of this quantity in predicting the SFR. The fit to SFE vs. $\Sigma_{\rm star}$ gives a slope of 0.75±0.01 with the ordinary least square bisector method (Isobe et al. 1990). As shown in Figure 5, below SFE of $10^{-9.8}$ yr^{-1} (horizontal dashed line), the slope becomes much steeper for the KS law, consistent with what found in Bigiel et al. (2008). On the other hand, such a large deviation is not seen for the extended Schmidt law. This further suggests the universality of the extended Schmidt law at sub-kpc resolution.

Many previous spatially-resolved studies of nearby galaxies have also noticed the trend of SFR as a function of stars. Ryder & Dopita (1994) found that the Hα emission spatially follows the distribution of I-band stellar emission in spiral disks. Their quantitative result gives $\Sigma_{\rm H\alpha} \propto \Sigma_{\rm I-band}^{0.64\pm0.37}$ within and among galaxies. In the LSB galaxies, Hunter et al. (1998) also found that the radial profile of the SFR follows that of the stellar mass density but not the gas density profile. Several other works have also noticed similar clues about the relationship between existing stars and star formation (Brosch et al. 1998; Hunter & Elmegreen 2004). Recently, Leroy et al. (2008) have also pointed out a correlation between the SFE and stellar density but claimed different slopes (see their Figure 3): a slope of unity in the HI-dominated regime with $1 < \log(\frac{\Sigma_{\rm star}}{\rm M_\odot pc^{-2}}) < 1.9$ and a constant trend (zero slope) in the H_2-dominated regime of $\log(\frac{\Sigma_{\rm star}}{\rm M_\odot pc^{-2}}) > 1.9$. We re-analyzed their data and found two factors that cause this inconsistency. We note that the unity slope in that work is not from a fit and the overall variation in the SFE at $1 < \log(\frac{\Sigma_{\rm star}}{\rm M_\odot pc^{-2}}) < 1.9$ is almost a factor of 10, too large to constrain the slope. A direct fit to all of their data points gives a slope of 0.65, close to our value. Also, they do not account for the color gradient in their stellar mass measurements, which would steepen the intrinsic slope. All these works together strongly demonstrate the existence of the SFE as a function of the stellar mass at sub-kpc resolution, while ours further indicate its significantly smaller scatter compared to the KS law.

4. DISCUSSION

4.1. *Test Of Theoretical Models Of The Star Formation Recipe*

4.1.1. *Is the extended Schmidt law just another form of the KS law?*

Can the extended Schmidt law be a result of the KS law and the relation between gas and stellar densities? Figure 6 shows the relation between $\Sigma_{\rm gas}$ and $\Sigma_{\rm star}$. Excluding the LSB and early-type objects, the gas density scales with the stellar density with an observed scatter of 0.5 dex. If the extended Schmidt law is derived from the KS law and the $\Sigma_{\rm gas}$-$\Sigma_{\rm star}$, it should have a scatter of 0.7

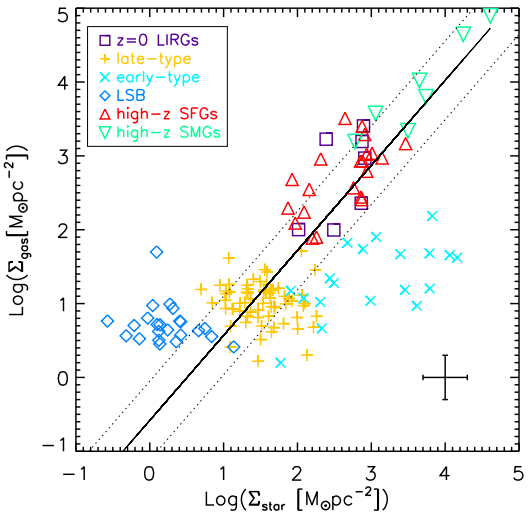

FIG. 6.— The stellar mass surface density vs. gas surface density. The solid line is the fit to galaxies excluding LSB and early-type ones. The dotted lines is the observed 1-σ scatter.

dex given the scatter of the SFE-$\Sigma_{\rm gas}$ relation of 0.5 dex, whereas the observed scatter of the extended Schmidt law is only 0.4 dex as listed in Table 4. This suggests that the KS law and $\Sigma_{\rm gas}$-$\Sigma_{\rm star}$ relations are not fundamental relations that drive the SFE-$\Sigma_{\rm gas}$ one. Stronger evidence comes from the LSB galaxies which do not follow either KS law or $\Sigma_{\rm gas}$-$\Sigma_{\rm star}$ relation but do follow the SFE-$\Sigma_{\rm gas}$ relation. In addition, the early-type galaxies also seems offset from the $\Sigma_{\rm gas}$-$\Sigma_{\rm star}$ relation but they do follow the extended Schmidt law. By invoking a different physical parameter ($\Sigma_{\rm star}$), the extended Schmidt law presents another star formation law that is not a simple recasting of the KS relation. In the remainder of this section, we will test several simple physical star formation models in order to understand its origin.

4.1.2. *Free-fall In A Star-Dominated Potential*

While the KS law can be interpreted as a free-fall in a gas-dominated gravitational potential, we note that the extended Schmidt law is consistent with the idea of free-fall in a stellar potential. The SFR can be expressed as the amount of gas collapsing into stars within a given timescale:

$$\Sigma_{\rm SFR} = \frac{\eta\Sigma_{\rm gas}}{\tau} \tag{8}$$

where η gives the fraction of the total gas that collapses into stars and τ describes the duration of gas collapse. A free-fall gas collapse in a star-dominated potential has a timescale:

$$\tau_{\rm ff} = \frac{1}{4}\sqrt{\frac{3\pi}{2G(\rho_{\rm gas}+\rho_{\rm star})}} \approx \frac{1}{4}\sqrt{\frac{3\pi}{2G\rho_{\rm star}}} = \frac{1}{4}\sqrt{\frac{3\pi h_{\rm star}}{G\Sigma_{\rm star}}}$$
$$= 3.5\times10^{8}{\rm yr}\left(\frac{h_{\rm star}}{1{\rm kpc}}\right)^{0.5}\left(\frac{1{\rm M}_\odot{\rm pc}^{-2}}{\Sigma_{\rm star}}\right)^{0.5} \tag{9}$$

where $\rho_{\rm gas}$, $\rho_{\rm star}$, $\Sigma_{\rm star}$ and $h_{\rm star}$ are the gas mass volume density, stellar mass volume density, stellar mass surface density and the stellar scale height, respectively. For a self-gravitating stellar disk, $\Sigma_{\rm star}$= $2\rho_{\rm star}h_{\rm star}$. This simple interpretation predicts the observed power index of 0.5 for $\Sigma_{\rm star}$, if $\rho_{\rm star} \gg \rho_{\rm gas}$ and $h_{\rm star}$ = constant. The comparison of Equation 8 to the observed relation gives:

$$\eta \approx 2\% \tag{10}$$

How well does this scenario represent reality? How does the stellar potential act on the gas collapse? As shown above, the above derivation assumes two conditions $h_{\rm star}$ = constant and $\rho_{\rm star} \gg \rho_{\rm gas}$. While there is evidence that the stellar scale height remains constant with radius within a galaxy (van der Kruit & Searle 1981; Fry et al. 1999), the variation among galaxies may contribute to the scatter of the correlation under this interpretation. The condition of $\rho_{\rm star} \gg \rho_{\rm gas}$ is true for general high-surface-brightness galaxies but not for LSB ones as shown in Figure 6 which shows that the gas potential dominates over the stellar one. If the gas density is included in the correlation as SFE $\propto (\Sigma_{\rm gas}+\Sigma_{\rm star})^{0.5}$, the correlation will not improve, but instead LSB galaxies will be offset toward the high density end. There is no room for additional gas self-gravity in the empirical relation.

4.1.3. *Pressure-Regulated H_2 Formation*

The prerequisite to star formation is formation of cold molecular H_2. Many works have highlighted the role of the stellar gravity in regulating H_2 formation (Elmegreen 1993; Wong & Blitz 2002; Blitz & Rosolowsky 2004, 2006). We explore here whether the extended Schmidt law actually reflects the process of H_2 production from HI. Quantitatively, the H_2-to-HI mass ratio ($R_{\rm mol}$) can be written as a function of pressure with a power index of γ:

$$R_{\rm mol} = {\rm H_2/HI} \propto P_{\rm ext}^{\gamma} \tag{11}$$

Blitz & Rosolowsky (2004) estimate the external pressure $P_{\rm ext}$ as the mid-plane pressure in an infinite two-fluid isothermal disk where the gas scale height is much less than the stellar height:

$$P_{\rm ext} = (2G)^{0.5}\Sigma_{\rm gas}v_{\rm gas}[\rho_{\rm star}^{0.5} + (\frac{\pi}{4}\rho_{\rm gas})^{0.5}]$$
$$= 0.84(G\Sigma_{\rm star})^{0.5}\Sigma_{\rm gas}\frac{v_{\rm gas}}{h_{\rm star}^{0.5}}$$
$$= (272{\rm cm}^{-3}{\rm K})(\frac{\Sigma_{\rm gas}}{{\rm M}_\odot{\rm pc}^{-2}})(\frac{\Sigma_{\rm star}}{{\rm M}_\odot{\rm pc}^{-2}})^{0.5}$$
$$(\frac{v_{\rm gas}}{{\rm kms}^{-1}})(\frac{h_{\rm star}}{\rm pc})^{-0.5}(k) \tag{12}$$

where $\Sigma_{\rm gas}$ is the mid-plane gas surface density, $v_{\rm gas}$ is the vertical velocity dispersion of the gas disk, $\rho_{\rm star}$ is the mid-plane stellar volume density, $\rho_{\rm gas}$ is the mid-plane gas volume density, $\Sigma_{\rm star}$ is the mid-plane stellar surface density, $h_{\rm star}$ is the stellar scale height and k is the Boltzmann constant. By assuming constant $v_{\rm gas}$ for the gas disk and constant $h_{\rm star}$ for the stellar disk, the Equation 11 has been demonstrated observationally with γ around 1.0 (Blitz & Rosolowsky 2006). Under this assumption and that stars form from molecular gas, the star formation prescription can be written as:

$$\Sigma_{\rm SFR} = \frac{\eta_{\rm H_2}\Sigma_{\rm H_2}}{\tau} = \frac{\eta_{\rm H_2}}{\tau}\frac{R_{\rm mol}}{1+R_{\rm mol}}\Sigma_{\rm gas}$$
$$= \frac{\eta_{\rm H_2}}{\tau}\frac{(P_{\rm ext}/P_0)^{\gamma}}{1+(P_{\rm ext}/P_0)^{\gamma}}\Sigma_{\rm gas} \tag{13}$$

where $\eta_{\rm H_2}$ is the fraction of the molecular gas that is locked in stars, τ is the timescale for the collapse of molecular clouds to stars, γ=0.92 and P_0/k is 4.3×10^4 cm^{-3} K as given by observation in Blitz & Rosolowsky (2006). The $\frac{\eta_{\rm H_2}}{\tau}$ is observed to be a constant (e.g. Gao & Solomon 2004; Wu et al. 2005; Leroy et al. 2008; Genzel et al. 2010). We now discuss $\Sigma_{\rm SFR}$ in two extreme pressure regimes:

HI-dominated galaxies ($P_{\rm ext}/P_0 \ll 1$, $R_{\rm mol} \ll 1$): The above equation gives

$$\Sigma_{\rm SFR} \propto (P_{\rm ext}/P_0)^{\gamma}\Sigma_{\rm gas} \propto \Sigma_{\rm star}^{0.5\gamma}\Sigma_{\rm gas}^{1.0+\gamma} \quad (14)$$

for constant $h_{\rm star}$ and $v_{\rm gas}$. At γ =0.92, the above equation predicts roughly the same power index for the $\Sigma_{\rm star}$ as we observe but almost two times larger for that of $\Sigma_{\rm gas}$.

H_2-dominated galaxies ($P_{\rm ext}/P_0 \gg 1$, $R_{\rm mol} \gg 1$): It is obvious in this regime there is no dependence of $\Sigma_{\rm SFR}$ on $\Sigma_{\rm star}$, inconsistent with the extended Schmidt law for H_2-dominated circumnuclear star-forming regions and LIRGs.

4.1.4. *Pressure-Supported Star Formation*

The scenario of pressure-supported star formation assumes that star formation is regulated by the pressure balance between gas collapse and feedback from stars (Thompson et al. 2005), i.e., weak stellar feedback leaves the gas collapse unimpeded, resulting in enhanced star formation, which in turn increases the feedback to prevent the further gas collapse; strong feedback prevents the efficient gas collapse, which lowers the amount of newly-formed stars and thus decreases the feedback strength. Quantitatively, we have

$$P_{\rm ext} = P_{\rm SFR} \quad (15)$$

Thompson et al. (2005) estimates the total pressure from star formation as a sum of the supernovae feedback and radiation pressure:

$$\begin{aligned} P_{\rm SFR} &\approx (P_{\rm SN} + P_{\rm RP}) \approx (5n_1^{-1/4}E_{51}^{13/14} + 1)P_{\rm RP} \\ &\approx (5n_1^{-1/4}E_{51}^{13/14} + 1)\epsilon c\Sigma_{\rm SFR} \end{aligned} \quad (16)$$

where $P_{\rm SN}$ is the pressure from supernova, $P_{\rm RP}$ is the radiation pressure from massive stars, n_1 is the density of the interstellar medium in the unit of 1 cm^{-3}, E_{51} is the supernova energy in the unit of 10^{51} ergs, ϵ is the conversion efficiency from the stellar mass into radiation ($\epsilon \sim 10^{-3}$ for a Salpeter initial mass function) and c is the speed of light. In general quiescent galaxies, the ISM density is low and the pressure is dominated by supernova while in LIRGs the radiation pressure starts to become important or even dominates.

Using the Equation 12 for $P_{\rm ext}$, we have

$$\begin{aligned} \frac{\Sigma_{\rm SFR}}{\rm M_\odot yr^{-1}pc^{-2}} = &\frac{1.9\times10^{-10}}{(5n_1^{-1/4}E_{51}^{13/14}+1)}(\frac{\Sigma_{\rm gas}}{\rm M_\odot pc^{-2}}) \\ &(\frac{\Sigma_{\rm star}}{\rm M_\odot pc^{-2}})^{0.5}(\frac{v_{\rm gas}}{\rm kms^{-1}})(\frac{h_{\rm star}}{\rm pc})^{-0.5} \end{aligned} \quad (17)$$

Comparing to the observed correlation (Equation 22), the above equation produces not only the exact power indices for both $\Sigma_{\rm star}$ and $\Sigma_{\rm gas}$ but also a similar constant. The caveat to this explanation is again offered by the LSB galaxies where the gas gravity cannot be neglected compared to the stellar term as shown in Figure 6 and as discussed above.

4.1.5. *Summary: Causal or Casual*

We compare the extended Schmidt law to some physical star-formation models including gas free-fall in the stellar potential, pressure-regulated H_2 formation and pressure-supported star formation. All of them invoke roles of the existing stars in star formation through stellar gravity on gas, and the first and third ones predict not only the same power indices but also similar normalizations to those observed ones. However, as pointed above, the assumption that stars dominate the mass seems unreasonable for the LSB galaxies at least in case of hydrostatic equilibrium. However, the stellar gravity can affect gas motion critically in configurations where stars show spatial and velocity differences from gas, such as stellar bars. An example of this may be seen in the numerical simulation of gas-dominated merging galaxies (Hopkins et al. 2009a,b). Springel & Hernquist (2005) and Robertson et al. (2006) have shown that gas-rich mergers result in disk galaxies instead of elliptical galaxies. The reason for this is not just that gas-rich mergers have too much gas to consume but also that they lack existing stars. Stars are collisionless and can relax its orbits violently during merging. Gas, on the other hand, is collisional and cannot relax rapidly, requiring angular momentum to be removed in order to form stars (Hopkins et al. 2009a). With non-axisymmetric distortion as induced by the secondary galaxy, the gravity of these stars thus provides the most efficient way to remove the gaseous angular momentum. Its efficiency far exceeds those of shock compression, gravity of the secondary galaxy and self gravity of the gas itself. Hopkins et al. (2009b) have derived an analytic expression that captures the role of existing stars: $f_{\rm starburst}/f_{\rm gas} \propto f_{\rm star}$, where $f_{\rm starburst}$ is the fraction of the total mass that forms stars, $f_{\rm gas}$ is initial gas mass fraction and $f_{\rm star}$ is initial stellar mass fraction. Determining whether similarly critical influence of stars on gas flow and processing also obtains in LSB and normal galaxies will probably require extensive simulations.

Since the physical models of star formation do not translate directly into the extended Schmidt law, one is not free to interpret the latter as a causal formula suggesting that stellar gravity regulates SFE. Instead, $\Sigma_{\rm star}$ may be a proxy for other physical parameters or a combination thereof, signifying regulation by more subtle or complex physics. $\Sigma_{\rm star}$ may represent the total kinetic and/or radiation energy dumped into the ISM by stars or the total metal enrichment over the galaxy's history. For example, the metal abundance is critical in ISM cooling and formation of dust grains on which H_2 can form efficiently. Theoretical models do confirm the significant deviation of the KS law in the low metallicity environment (Krumholz et al. 2009; Gnedin & Kravtsov 2010; Papadopoulos & Pelupessy 2010).

4.2. *Implications For the Star-Forming Main Sequence*

We here discuss the implication of the extended Schmidt law for galaxy formation and evolution with focus on the main sequence of star-forming galaxies. Studies have shown that stars form mainly in the blue star-forming galaxies while there is little star formation in red galaxies. Such a bi-modality has been well established through various observations (e.g. Blanton et al.

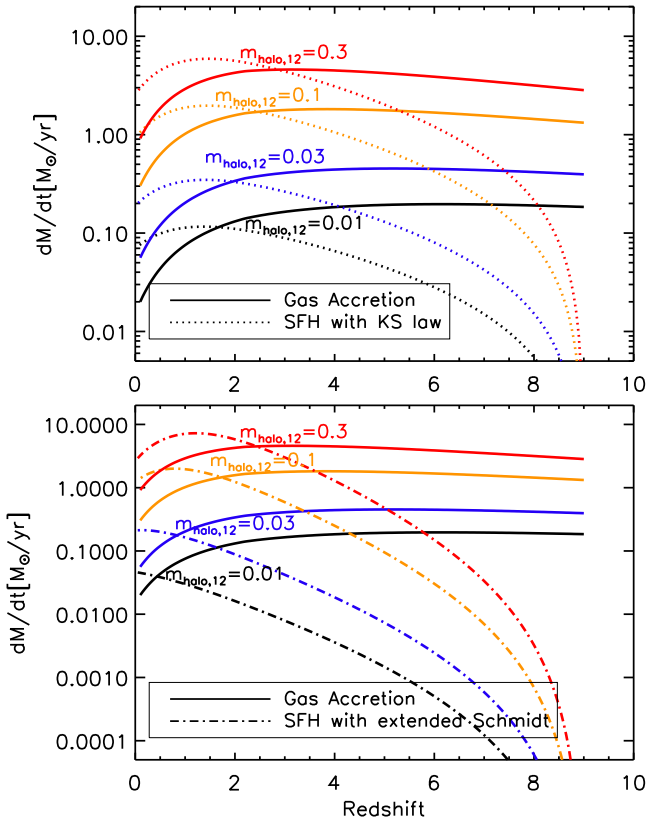

FIG. 7.— Upper: The SFR histories (dotted lines) as predicted by the KS law for given gas accretion histories (solid lines with the same colors) in four different halo masses where $m_{\rm halo,12}$ is the halo mass at z=0 in the unit of 10^{12} $M_\odot$. Lower: The SFR histories with the extended Schmidt law.

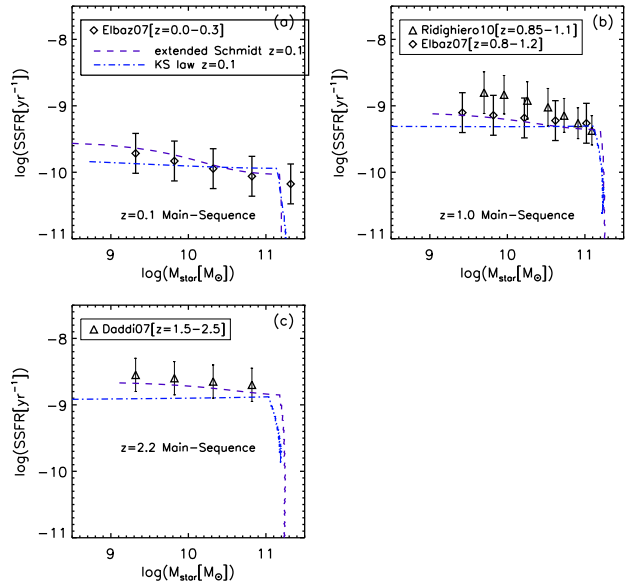

FIG. 8.— The observed star-forming main-sequence from z=0 to z=2 compared to the predictions by implementing the extended Schmidt law (dashed lines) and the KS law (dotted-dashed lines) into the analytic model of gas accretion in the Λ CDM cosmology.

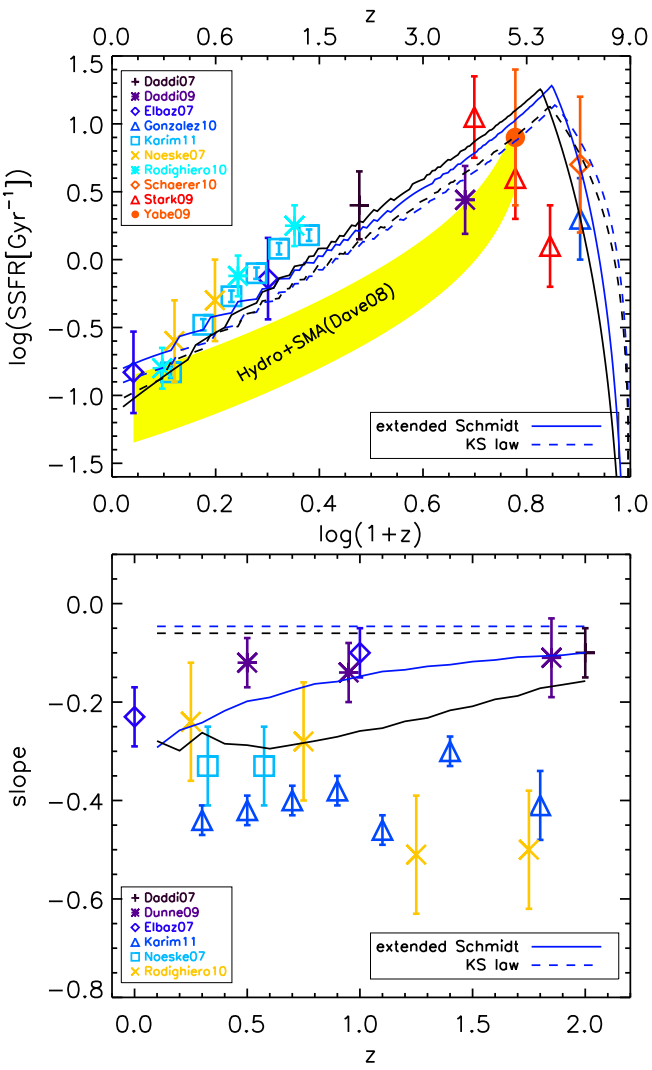

FIG. 9.— Upper panel: The observed evolution of the SSFR (specific star formation rate) for $M_{\rm star}$=10^{10} $M_\odot$ compared to the predictions by the extended Schmidt (solid lines) and KS laws (dashed lines). The data are taken directly from the literature except for Stark et al. (2009) where we further correct the extinction according to the luminosity- and redshift-dependent extinction correction curve of Bouwens et al. (2009). "SMA" stands for the semi-analytic model. Lower Panel: The evolution of the observed slope (specific SFR $\propto M_{\rm star}^{\rm slope}$) as a function of the redshift from different studies. The solid and dashed line show the result for the extended and KS laws, respectively, while the blue and black color indicate the galaxy size evolution of $\propto (H(z=4)/H(z))$ and $\propto (H(z=4)/H(z))^{0.4}$, respectively.

2003). While red galaxies show a relation between the UV/optical color and luminosity, the SFRs of blue galaxies are found to correlate with stellar masses, a relationship with a slope a bit below unity and a small dispersion of $\lesssim$ 0.3 dex (Brinchmann et al. 2004; Elbaz et al. 2007; Daddi et al. 2007; Zheng et al. 2007; Noeske et al. 2007a; Chen et al. 2009; Oliver et al. 2010; Rodighiero et al. 2010). This so-called main sequence of star-forming galaxies and its evolution have provided important constraints on the mechanism driving the rapid evolution of the cosmic SFR density. For example, an evolving stellar IMF is able to explain the evolution of the main sequence as proposed by Davé (2008). A more general interpreta-

tion would attempt to quantify the star formation history (SFH), since

$$M_{\rm star}(z_0) \propto \int_{z_{\rm form}}^{z_0} SFR(z)dz = SFR(z_0)\int_{z_{\rm form}}^{z_0} \frac{SFR(z)}{SFR(z_0)}dz$$
$$= SFR(z_0)\int_{z_{\rm form}}^{z_0} SFH(z)dz \quad (18)$$

where z_0 is the observed redshift of a galaxy, $z_{\rm form}$ is the redshift where the galaxy starts to form and SFH is the star-formation history normalized by the current SFR. Current numerical simulations and analytic models have difficulties in producing the observed slope below unity without invoking ad hoc mechanisms to delay star formation in low mass systems (Noeske et al. 2007b; Davé 2008; Bouché et al. 2010). This can be seen from Equation 18. If all galaxies have a similar smooth shape of SFH and form at the same redshift, then Equation 18 gives a slope of unity. To have a shallower slope, the integral of the SFH normalized by the current SFR needs to be smaller for a lower mass galaxy (see Equation 18), for example, $z_{\rm form}$ can be lower for a lower mass galaxy. This can be also rephrased as shorter characteristic star-formation timescale or late onset of star formation in a lower mass galaxy. However, in numerical simulations and semi-analytic models, the gas accretion is determined by the well-known dark matter halo growth in Λ CDM cosmology. Thus SFH is not a free parameter to adjust (Davé 2008). The growth of the dark matter halo follows $\dot{M}_{\rm halo} \propto M_{\rm halo}^s$ with s above unity (e.g. Neistein & Dekel 2008), which would result in a slope of the main-sequence above unity if the SFR follows that of the dark matter halo growth. In current models, ad-hoc mechanisms are thus proposed to delay star formation in low mass galaxies, such as, a very strong feedback or a mass floor below which the gas cannot be accreted (e.g. Davé 2008; Bouché et al. 2010). Compared to the KS law that is now widely invoked in numerical simulations and semi-analytic models, the extended Schmidt law indicates a slow SFR increase at early times due to the lack of existing stars and fast evolution at late times for a given gas accretion history. This introduces naturally a *delayed* onset of star formation in a low-mass galaxy, which is the key to explaining the star-forming main sequence with a slope below unity. In the following, we show quantitatively that the delayed star formation in a low mass system is a natural result of star formation that is governed by the extended Schmidt law.

We follow exactly Bouché et al. (2010) to construct the growth of the dark matter halo and gas accretion. For a given gas accretion history, star formation occurs following either the extended Schmidt law or the KS law. To apply these two laws, we assume the evolution of the half-light radius ($R_{1/2}$) from Papovich et al. (2010). The numerical calculations include:

(1) The dark matter halo growth rate follows:

$$\dot{M}_{\rm halo} = 510 M_{\rm halo,12}^s((1+z)/3.2)^t \ {\rm M_\odot/yr} \quad (19)$$

where $M_{\rm halo,12} = M_{\rm halo}/10^{12}M_\odot$, s=1.1 and t=2.2.

(2) The gas accretion rate is given by:

$$\dot{M}_{\rm gas,in} = \epsilon_{\rm in} f_{\rm b} \dot{M}_{\rm halo} \quad (20)$$

Similar to Bouché et al. (2010), $f_{\rm b}$ is the baryonic fraction of 0.18. $\epsilon_{\rm in}$ is the accretion efficiency that is equal to 0.7 at z > 2.2 where cold accretion mode dominates. Due to accumulation of stars and hot gas, the accretion efficiency must decrease with time. For $z <$ 2.2, Bouché et al. (2010) simply assumed $\epsilon_{\rm in}$=f(z)×0.7 where $f(z)$ is a linear function of time with f(2.2)=1 and f(0)=0.5. For $M_{\rm halo}$ above 10^{12} $M_\odot$ where the cold mode accretion is not important, $\epsilon_{\rm in}$=0 as discussed by Bouché et al. (2010). However, we do not introduce a low-mass floor ($M_{\rm halo}$=10^{11} $M_\odot$) below which $\epsilon_{\rm in}$=0, which is used to fit the observed main-sequence as shown by Bouché et al. (2010). This is the main difference of our model besides adopting the extended Schmidt law.

(3) At each redshift, the net gas accretion is given by

$$\dot{M}_{\rm gas} = \dot{M}_{\rm gas,in} - (1-R)\times SFR - \dot{M}_{\rm gas,out} \quad (21)$$

where R is the recycled gas fraction and equal to 0.52 for a Chabrier IMF in this study. $\dot{M}_{\rm gas,out}$=a×SFR is the gas outflow where a is set to be zero by assuming the outflow eventually falls back to form stars. Unlike the above two equations (19, 20) that are solely determined by the dark matter growth, this equation will produce different results for different star formation laws.

(4) Star formation follows either the extended Schmidt law:

$$\frac{\rm SFE}{\rm yr^{-1}} = 10^{-10.28}(\frac{\Sigma_{\rm star}}{\rm M_\odot pc^{-2}})^{0.48} \quad (22)$$

or the KS law (using the exponent from the fit in this study):

$$\frac{\Sigma_{\rm SFR}}{\rm M_\odot/yr/pc^2} = 10^{-9.90}(\frac{\Sigma_{\rm gas}}{\rm M_\odot/pc^2})^{1.38} \quad (23)$$

where $\Sigma = \frac{0.5M}{\pi R_{1/2}^2}$. Following Papovich et al. (2010), the half light radius $R_{1/2}(z)$ is given by

$$\frac{R_{1/2}}{\rm kpc} = 1.7\frac{H(z=4)}{H(z)} \quad (24)$$

where $H(z=4)$=430 km/s/Mpc.

The above six equations are solved numerically with the formation $z_{\rm form}$=9 where the initial gas and stellar mass are set to zero, and a series of initial dark matter masses are assumed. Examples of gas accretion and SFR histories are shown in Figure 7 for both KS and extended Schmidt laws. With the KS law, star formation responds only to the accumulated gas and thus quickly reaches the state where the SFR follows more or less the gas accretion history at later times (e.g. Papovich et al. 2010). As shown in Figure 7, the SFHs of different mass systems are quite similar at z<7 with similar peak redshift and slopes at both sides. This implies a unity slope of star-forming main sequence as indicated by Equation 18. On the other hand, the SFH given by the extended Schmidt law slowly increases at early time and it is slower for lower mass systems simply as a result of smaller existing stellar populations. The SFHs peak at lower redshift for lower mass systems as shown in Figure 7, which naturally introduces a delay mechanism that is required to explain the main sequence. The quantitative comparisons to the observed main sequences in term of SSFR (specific star formation rate) vs. $M_{\rm star}$ are shown in Figure 8. While both relations produce more or less the correct normalizations, the KS law never produces a negative slope while the prediction by the extended Schmidt law is consistent with the

observed data from z=0 all the way up to z=2. Such a consistency is reached without introducing ad hoc mechanisms to delay star formation in low mass systems, unlike other studies based on the KS law (Noeske et al. 2007b; Davé 2008; Bouché et al. 2010). Figure 9 collects current studies of the SSFR evolution including both normalization at $\log M_{\rm star}/M_{\odot}$=10 and the slope. In general, these two relations (extended Schmidt and KS laws), as well as the numerical simulations, all predict the rapid evolution of the SSFR, which reflects the gas accretion history. Among them, the extended Schmidt law produces the best match to the observed data, although the discrepancy still exists at high z (z>3). As shown in the lower panel of Figure 9, although different slopes of the main sequence have been observed by different studies, all of them are negative. It is clearly shown that the extended Schmidt law produces much more consistent values with the observed data compared to the KS law. The above result about the predicted slope by the KS law depends little on the numerical values of the physical parameters invoked in Equation 19-24, except for the s parameter that is unlikely to be below unity. A steeper slope by the extended Schmidt law can be produced if the galaxy size evolves slower ($\propto (H(z=4)/H(z))^{0.4}$) shown as black lines in the figure.

Recently, Dutton et al. (2010) have re-produced the observed main sequence through the semi-analytical model with the star formation recipe of the pressure-regulated H_2 formation. The resulting two-power-law star formation relation has the same slope as the KS one at the high density regime but a much steeper slope (2.84) at the low density end. This further indicates that the pure KS law over-predicts the SFR at the early stage of galaxy evolution. Without imposing ad hoc mechanisms to delay star formation in a low mass system, the extended Schmidt law does provide a new way to understand the star-forming main sequence and its evolution.

5. CONCLUSIONS

(1) We demonstrate empirically the existence of a tight correlation between the star formation efficiency (SFE=$\Sigma_{\rm SFR}/\Sigma_{\rm gas}$) and the stellar mass density ($\Sigma_{\rm star}$), referred as the extended Schmidt law. The correlation was derived by looking for the dependence of $\Sigma_{\rm SFR}$ on $\Sigma_{\rm gas}$ and $\Sigma_{\rm star}$. It has a power index of 0.48±0.04 and holds over 5 orders of magnitude in the stellar mass density for various types of galaxies including the low-surface-brightness (LSB) ones that deviate significantly from the Kennicutt-Schmidt law.

(2) We further show that the extended Schmidt law also applies to spatially resolved regions at sub-kpc resolution. In a sample of 12 spiral galaxies, the extended Schmidt law not only holds for LSB regions but also shows significantly smaller scatters, a factor of 1.5 and 3 smaller within and across galaxies, respectively, compared to the Kennicutt-Schmidt law.

(3) The extended Schmidt law may suggest a critical role for existing stellar populations in on-going star formation activity. Alternatively, it may be a manifestation of more complex physics where $\Sigma_{\rm star}$ is a proxy for other variables or processes. The comparison of the extended Schmidt law to several simple physical models indicates that models of gas free-fall in stellar gravitational potential and pressure-supported star formation produce not only the same power index but also a similar normalization. However, this success is limited to some cases, and the exact physical interpretation of the extended Schmidt law needs further exploration.

(4) By applying this extended Schmidt law to an analytic model of gas accretion in Λ CDM cosmology, the observed main sequence of star-forming galaxies is well reproduced in the model without the need for ad hoc mechanisms to delay star formation in low mass systems.

6. ACKNOWLEDGMENT

We thank the anonymous referee for the detailed and constructive comments. We also thank Daniel Dale, Leslie K. Hunt, Eva Schinnerer and Bruce G Elmegreen for careful reading and comments. The work is supported through the Spitzer 5MUSES Legacy Program 40539. The authors acknowledge support by NASA through awards issued by JPL/Caltech. This work was based on observations made with the Spitzer Space Telescope, which is operated by JPL/Caltech under a contract with NASA. This research has made use of the NASA/IPAC Extragalactic Database (NED) which is operated by the Jet Propulsion Laboratory, California Institute of Technology, under contract with the National Aeronautics and Space Administration. Funding for the SDSS and SDSS-II has been provided by the Alfred P. Sloan Foundation, the Participating Institutions, the National Science Foundation, the U.S. Department of Energy, the National Aeronautics and Space Administration, the Japanese Monbukagakusho, the Max Planck Society, and the Higher Education Funding Council for England. The SDSS Web Site is http://www.sdss.org/.

REFERENCES

Bigiel, F., Leroy, A., Walter, F., Brinks, E., de Blok, W. J. G., Madore, B., & Thornley, M. D. 2008, AJ, 136, 2846
Blanton, M. R., et al. 2003, ApJ, 594, 186
Blitz, L., & Rosolowsky, E. 2004, ApJ, 612, L29
Blitz, L., & Rosolowsky, E. 2006, ApJ, 650, 933
Boissier, S., Prantzos, N., Boselli, A., & Gavazzi, G. 2003, MNRAS, 346, 1215
Bouché, N., et al. 2010, ApJ, 718, 1001
Bouwens, R. J., et al. 2009, ApJ, 705, 936
Brinchmann, J., Charlot, S., White, S. D. M., Tremonti, C., Kauffmann, G., Heckman, T., & Brinkmann, J. 2004, MNRAS, 351, 1151
Brosch, N., Heller, A., & Almoznino, E. 1998, ApJ, 504, 720
Bruzual, G., & Charlot, S. 2003, MNRAS, 344, 1000
Bryant, P. M., & Scoville, N. Z. 1999, AJ, 117, 2632
Bruzual A, G. 2007, arXiv:astro-ph/0703052
Chabrier, G. 2003, PASP, 115, 763
Chen, Y.-M., Wild, V., Kauffmann, G., Blaizot, J., Davis, M., Noeske, K., Wang, J.-M., & Willmer, C. 2009, MNRAS, 393, 406
Crosthwaite, L. P., & Turner, J. L. 2007, AJ, 134, 1827
Courteau, S. 1996, ApJS, 103, 363
Cox, A. L., Sparke, L. S., Watson, A. M., & van Moorsel, G. 2001, AJ, 121, 692
Crocker, A. F., Bureau, M., Young, L. M., & Combes, F. 2011, MNRAS, 410, 1197
Daddi, E., et al. 2007, ApJ, 670, 156
Daddi, E., et al. 2010, ApJ, 713, 686
Daddi, E., et al. 2010, ApJ, 713, 686
Davé, R. 2008, MNRAS, 385, 147

de Vaucouleurs, G., de Vaucouleurs, A., & Corwin, H. G. 1976, University of Texas Monographs in Astronomy, Austin: University of Texas Press, 1976,
Dickman, R. L., Snell, R. L., & Schloerb, F. P. 1986, ApJ, 309, 326
Downes, D., & Solomon, P. M. 1998, ApJ, 507, 615
Dunne, L., et al. 2009, MNRAS, 394, 3
Dutton, A. A., van den Bosch, F. C., & Dekel, A. 2010, MNRAS, 405, 1690
Elbaz, D., et al. 2007, A&A, 468, 33
Elmegreen, B. G. 1993, ApJ, 411, 170
Elmegreen, B. G., & Parravano, A. 1994, ApJ, 435, L121
Elmegreen, B. G. 1997, ApJ, 486, 944
Erb, D. K., Steidel, C. C., Shapley, A. E., Pettini, M., Reddy, N. A., & Adelberger, K. L. 2006, ApJ, 646, 107
Fry, A. M., Morrison, H. L., Harding, P., & Boroson, T. A. 1999, AJ, 118, 1209
Gao, Y., & Solomon, P. M. 2004, ApJ, 606, 271
Genzel, R., et al. 2010, arXiv:1003.5180
Gil de Paz, A., et al. 2007, ApJS, 173, 185
Hainline, L. J., Blain, A. W., Smail, I., Alexander, D. M., Armus, L., Chapman, S. C., & Ivison, R. J. 2010, arXiv:1006.0238
Helfer, T. T., Thornley, M. D., Regan, M. W., Wong, T., Sheth, K., Vogel, S. N., Blitz, L., & Bock, D. C.-J. 2003, ApJS, 145, 259
Hinz, J. L., Rieke, M. J., Rieke, G. H., Willmer, C. N. A., Misselt, K., Engelbracht, C. W., Blaylock, M., & Pickering, T. E. 2007, ApJ, 663, 895
Ho, L. C., Filippenko, A. V., & Sargent, W. L. W. 1997, ApJ, 487, 591
Hollenbach, D. J., & Tielens, A. G. G. M. 1999, Reviews of Modern Physics, 71, 173
Hopkins, P. F., et al. 2009a, MNRAS, 397, 802
Hopkins, P. F., Cox, T. J., Younger, J. D., & Hernquist, L. 2009b, ApJ, 691, 1168
Hunter, D. A., Elmegreen, B. G., & Baker, A. L. 1998, ApJ, 493, 595
Hunter, D. A., & Elmegreen, B. G. 2004, AJ, 128, 2170
Irwin, J. A., Seaquist, E. R., Taylor, A. R., & Duric, N. 1987, ApJ, 313, L91
Isobe, T., Feigelson, E. D., Akritas, M. G., & Babu, G. J. 1990, ApJ, 364, 104
Jogee, S., Scoville, N., & Kenney, J. D. P. 2005, ApJ, 630, 837
Karim, A., Schinnerer, E., VLA-COSMOS, t., & COSMOS collaborations 2011, arXiv:1102.1423
Kelly, B. C. 2007, ApJ, 665, 1489
Kennicutt, R. C., Jr. 1989, ApJ, 344, 685
Kennicutt, R. C., Jr. 1998a, ApJ, 498, 541
Kennicutt, R. C., Jr. 1998b, ARA&A, 36, 189
Kennicutt, R. C., Jr., et al. 2003, PASP, 115, 928
Kennicutt, R. C., Jr., et al. 2007, ApJ, 671, 333
Kennicutt, R. C., et al. 2009, ApJ, 703, 1672
Knapp, G. R., & Raimond, E. 1984, A&A, 138, 77
Krumholz, M. R., McKee, C. F., & Tumlinson, J. 2009, ApJ, 699, 850
Leroy, A. K., Walter, F., Brinks, E., Bigiel, F., de Blok, W. J. G., Madore, B., & Thornley, M. D. 2008, AJ, 136, 2782
Maraston, C., Daddi, E., Renzini, A., Cimatti, A., Dickinson, M., Papovich, C., Pasquali, A., & Pirzkal, N. 2006, ApJ, 652, 85
Maraston, C., Pforr, J., Renzini, A., Daddi, E., Dickinson, M., Cimatti, A., & Tonini, C. 2010, MNRAS, 407, 830
Martin, C. L., & Kennicutt, R. C., Jr. 2001, ApJ, 555, 301
Matthews, L. D., Gao, Y., Uson, J. M., & Combes, F. 2005, AJ, 129, 1849
Neistein, E., & Dekel, A. 2008, MNRAS, 383, 615
Noeske, K. G., et al. 2007, ApJ, 660, L43
Noeske, K. G., et al. 2007, ApJ, 660, L47
Oliver, S., et al. 2010, MNRAS, 405, 2279
Oosterloo, T., et al. 2010, MNRAS, 409, 500
Papadopoulos, P. P., & Pelupessy, F. I. 2010, ApJ, 717, 1037
Papovich, C., Finkelstein, S. L., Ferguson, H. C., Lotz, J. M., & Giavalisco, M. 2010, arXiv:1007.4554
Paturel, G., Petit, C., Prugniel, P., Theureau, G., Rousseau, J., Brouty, M., Dubois, P., & Cambrésy, L. 2003, A&A, 412, 45
Robertson, B., Bullock, J. S., Cox, T. J., Di Matteo, T., Hernquist, L., Springel, V., & Yoshida, N. 2006, ApJ, 645, 986
Rodighiero, G., et al. 2010, A&A, 518, L25
Roychowdhury, S., Chengalur, J. N., Begum, A., & Karachentsev, I. D. 2009, MNRAS, 397, 1435
Ryder, S. D., & Dopita, M. A. 1994, ApJ, 430, 142
Sage, L. J., & Welch, G. A. 2006, ApJ, 644, 850
Schiminovich, D., et al. 2010, MNRAS, 1288
Schmidt, M. 1959, ApJ, 129, 243
Schuster, K. F., Kramer, C., Hitschfeld, M., Garcia-Burillo, S., & Mookerjea, B. 2007, A&A, 461, 143
Scoville, N. Z., Yun, M. S., & Bryant, P. M. 1997, ApJ, 484, 702
Sérsic, J. L., & Pastoriza, M. 1967, PASP, 79, 152
Shapiro, K. L., et al. 2010, MNRAS, 402, 2140
Solomon, P. M., Rivolo, A. R., Barrett, J., & Yahil, A. 1987, ApJ, 319, 730
Springel, V., & Hernquist, L. 2005, ApJ, 622, L9
Stark, D. P., Ellis, R. S., Bunker, A., Bundy, K., Targett, T., Benson, A., & Lacy, M. 2009, ApJ, 697, 1493
Shi, Y., Rieke, G., Donley, J., Cooper, M., Willmer, C., & Kirby, E. 2008, ApJ, 688, 794
Silk, J. 1997, ApJ, 481, 703
Swinbank, A. M., et al. 2010, MNRAS, 405, 234
Tacconi, L. J., et al. 2008, ApJ, 680, 246
Thompson, T. A., Quataert, E., & Murray, N. 2005, ApJ, 630, 167
Gnedin, N. Y., & Kravtsov, A. V. 2010, ApJ, 714, 287
Graciá-Carpio, J., Planesas, P., & Colina, L. 2007, A&A, 468, L67
van der Kruit, P. C., & Searle, L. 1981, A&A, 95, 105
van Driel, W., & van Woerden, H. 1991, A&A, 243, 71
Vázquez, G. A., & Leitherer, C. 2005, ApJ, 621, 695
Walter, F., Brinks, E., de Blok, W. J. G., Bigiel, F., Kennicutt, R. C., Thornley, M. D., & Leroy, A. 2008, AJ, 136, 2563
Wei, L. H., Vogel, S. N., Kannappan, S. J., Baker, A. J., Stark, D. V., & Laine, S. 2010, ApJ, 725, L62
Wong, T., & Blitz, L. 2002, ApJ, 569, 157
Wyder, T. K., et al. 2009, ApJ, 696, 1834
Wu, J., Evans, N. J., II, Gao, Y., Solomon, P. M., Shirley, Y. L., & Vanden Bout, P. A. 2005, ApJ, 635, L173
Yun, M. S., Scoville, N. Z., & Knop, R. A. 1994, ApJ, 430, L109
Yun, M. S., & Scoville, N. Z. 1995, ApJ, 451, L45
Zheng, X. Z., Bell, E. F., Papovich, C., Wolf, C., Meisenheimer, K., Rix, H.-W., Rieke, G. H., & Somerville, R. 2007, ApJ, 661, L41

TABLE 1
SAMPLES WITH CO AND HI DATA

name	type	red	Dist. [Mpc]	Aperture	Area [kpc^2]	log($\Sigma_{\rm SFR}$) [M$_\odot$/yr/kpc^2]	log($\Sigma_{\rm gas}$) [M$_\odot$/pc^2]	Ref$_{\rm sfr,gas}$	log($\Sigma_{\rm star}$) [M$_\odot$/pc^2]	Band$_{\rm stellar-mass}$	Ref$_{\rm star}$
(1)	(2)	(3)	(4)	(5)	(6)	(7)	(8)	(9)	(10)	(11)	(12)
NGC0224	late-type	-0.001001	0.78	R_{25}	1106.29	-3.31	0.81	1	2.00	IRAC3.6	18
NGC0598	late-type	-0.000597	0.80	R_{25}	133.25	-2.65	1.16	1	1.58	IRAC3.6	18
NGC0628	late-type	0.002192	7.30	$1.5R_{25}$	764.54	-2.98	0.90	2	1.22	IRAC3.6	2
NGC0772	late-type	0.008246	35.00	R_{25}	4231.16	-3.02	1.00	1	1.53	nuv,U,B,V,I,J,H,K	18
NGC1058	late-type	0.001728	9.37	R_{25}	52.65	-2.38	0.83	1	1.33	B,V,I,J,H,K	18
NGC1569	late-type	-0.000347	2.20	R_{25}	2.02	-0.98	1.45	1	2.24	nuv,U,B,V,J,H,K	18
NGC2336	late-type	0.007352	3.50	R_{25}	38.86	-2.10	1.00	1	1.22	U,B,V,J,H,K	18
NGC2403	late-type	0.000437	3.20	$1.5R_{25}$	376.68	-2.99	0.93	2	1.12	IRAC3.6	2
NGC2841	late-type	0.002128	14.10	$1.5R_{25}$	1425.31	-3.28	0.96	2	1.65	IRAC3.6	2
NGC2976	late-type	0.000010	3.60	$1.5R_{25}$	102.07	-3.07	0.41	2	1.09	IRAC3.6	2
NGC3031	late-type	-0.000113	3.50	R_{25}	402.25	-2.68	0.97	1	2.08	fuv,nuv,B,V,R,I,J,H,K,IRAC1	18
NGC3077	late-type	0.000047	3.80	$1.5R_{25}$	63.62	-2.87	1.30	2	1.50	IRAC3.6	2
NGC3184	late-type	0.001975	11.10	$1.5R_{25}$	1000.98	-3.05	0.75	2	1.30	IRAC3.6	2
NGC3198	late-type	0.002212	13.80	$1.5R_{25}$	1194.59	-3.11	1.04	2	1.02	IRAC3.6	2
NGC3310	late-type	0.003312	17.50	R_{25}	249.96	-1.32	1.26	1	1.07	U,B,V,J,H,K	18
NGC3338	late-type	0.004343	25.11	R_{25}	1462.36	-2.74	0.93	1	1.12	U,B,V,J,H,K	18
NGC3351	late-type	0.002595	10.10	$1.5R_{25}$	794.23	-2.93	0.51	2	1.50	IRAC3.6	2
NGC3368	late-type	0.002992	9.72	R_{25}	265.96	-2.73	1.00	1	2.10	nuv,U,B,V,J,H,K	18
NGC3486	late-type	0.002272	10.55	R_{25}	373.83	-2.64	1.01	1	0.85	nuv,U,B,V,J,H,K	18
NGC3521	late-type	0.002672	10.70	$1.5R_{25}$	1176.28	-2.75	1.08	2	1.63	IRAC3.6	2
NGC3627	late-type	0.002425	9.30	$1.5R_{25}$	1365.72	-2.79	0.22	2	1.46	IRAC3.6	2
NGC3631	late-type	0.003856	24.30	R_{25}	832.50	-1.91	1.20	1	1.32	B,V,J,H,K	18
NGC3675	late-type	0.002568	18.50	R_{25}	793.79	-2.19	1.04	1	1.93	B,I,J,H,K	18
NGC3726	late-type	0.002887	13.50	R_{25}	354.09	-2.46	1.16	1	1.31	B,V,J,H,K	18
NGC3893	late-type	0.003226	18.30	R_{25}	339.38	-2.14	1.15	1	1.57	B,J,H,K	18
NGC3938	late-type	0.002699	12.20	R_{25}	278.57	-2.29	1.25	1	1.32	fuv,nuv,B,V,R,I,J,H,K,IRAC1	18
NGC4178	late-type	0.001248	17.49	R_{25}	326.11	-2.45	1.25	1	0.95	B,V,J,H,K	18
NGC4189	late-type	0.007055	25.10	R_{25}	222.06	-2.27	1.18	1	1.64	B,V,J,H,K	18
NGC4214	late-type	0.000970	2.90	$1.5R_{25}$	59.45	-2.74	0.93	2	1.03	IRAC3.6	2
NGC4254	late-type	0.008029	20.00	R_{25}	720.65	-1.88	1.43	1	1.59	fuv,nuv,B,V,R,I,J,H,K,IRAC1	18
NGC4258	late-type	0.001494	7.30	R_{25}	809.58	-2.54	0.70	1	1.51	nuv,B,V,J,H,K	18
NGC4294	late-type	0.001184	17.98	R_{25}	134.62	-2.05	1.13	1	1.03	U,B,V,J,H,K	18
NGC4303	late-type	0.005224	17.50	R_{25}	710.29	-1.92	1.26	1	1.58	U,B,V,J,H,K	18
NGC4321	late-type	0.005240	20.00	R_{25}	1232.35	-2.25	1.21	1	1.74	fuv,nuv,B,V,R,I,J,H,K,IRAC1	18
NGC4394	late-type	0.003075	16.80	R_{25}	286.03	-3.06	0.67	1	1.68	U,B,V,J,H,K	18
NGC4402	late-type	0.000774	15.70	R_{25}	157.83	-2.98	1.10	1	1.82	nuv,B,J,H,K	18
NGC4449	late-type	0.000690	4.20	$1.5R_{25}$	55.42	-2.17	1.46	2	1.56	IRAC3.6	2
NGC4501	late-type	0.007609	10.50	R_{25}	264.45	-2.39	1.11	1	2.06	U,B,V,J,H,K	18
NGC4519	late-type	0.004056	27.89	R_{25}	498.06	-2.16	1.17	1	1.03	U,B,V,J,H,K	18
NGC4535	late-type	0.006551	17.50	R_{25}	809.87	-2.56	1.06	1	1.37	B,V,J,H,K	18
NGC4548	late-type	0.001621	17.50	R_{25}	530.73	-2.70	0.73	1	1.81	B,V,J,H,K	18
NGC4561	late-type	0.004693	12.30	R_{25}	19.76	-2.11	1.61	1	1.07	U,B,V,J,H,K	18
NGC4569	late-type	-0.000784	20.00	R_{25}	1663.31	-2.96	0.62	1	1.65	fuv,nuv,B,V,R,I,J,H,K,IRAC1	18
NGC4571	late-type	0.001141	17.50	R_{25}	279.34	-2.74	0.88	1	1.36	B,V,J,H,K	18
NGC4579	late-type	0.005060	20.00	R_{25}	693.20	-2.50	0.83	1	2.26	fuv,nuv,B,V,R,I,J,H,K,IRAC1	18
NGC4639	late-type	0.003395	22.28	R_{25}	241.11	-2.29	0.83	1	1.61	U,B,J,H,K	18
NGC4647	late-type	0.004700	17.50	R_{25}	235.88	-2.40	1.07	1	1.88	U,B,J,H,K	18
NGC4651	late-type	0.002628	25.95	R_{25}	549.63	-2.16	1.14	1	1.62	B,V,J,H,K	18
NGC4654	late-type	0.003489	17.50	R_{25}	377.29	-2.24	1.17	1	1.54	U,B,V,J,H,K	18
NGC4689	late-type	0.005390	17.50	R_{25}	310.36	-2.56	0.96	1	1.68	B,V,J,H,K	18
NGC4698	late-type	0.003366	25.10	R_{25}	574.66	-3.73	0.30	1	2.13	U,B,V,J,H,K	18
NGC4713	late-type	0.002175	17.05	R_{25}	130.93	-1.71	1.16	1	1.08	U,B,V,J,H,K	18

TABLE 1 — *Continued*

name	type	red	Dist. [Mpc]	Aperture	Area [kpc^2]	log($\Sigma_{\rm SFR}$) [M$_\odot$/yr/kpc^2]	log($\Sigma_{\rm gas}$) [M$_\odot$/pc^2]	Ref$_{\rm sfr,gas}$	log($\Sigma_{\rm star}$) [M$_\odot$/pc^2]	Band$_{\rm stellar-mass}$	Ref$_{\rm star}$
(1)	(2)	(3)	(4)	(5)	(6)	(7)	(8)	(9)	(10)	(11)	(12)
NGC4736	late-type	0.001027	4.70	$1.5R_{25}$	198.56	-2.62	0.66	2	2.00	IRAC3.6	2
NGC4826	late-type	0.001361	5.60	R_{25}	133.73	-2.65	0.68	1	2.22	fuv,nuv,B,V,R,I,J,H,K,IRAC1	18
NGC5033	late-type	0.002919	13.30	R_{25}	975.99	-2.82	1.01	1	1.29	fuv,nuv,B,V,R,I,J,H,K,IRAC1	18
NGC5055	late-type	0.001614	10.10	$1.5R_{25}$	2140.08	-3.00	0.92	2	1.47	IRAC3.6	2
NGC5194	late-type	0.001544	8.00	$1.5R_{25}$	572.56	-2.26	1.00	2	1.84	IRAC3.6	2
NGC5236	late-type	0.001711	4.64	R_{25}	173.57	-1.59	1.71	1	2.05	U,B,V,J,H,K	18
NGC5457	late-type	0.000804	6.00	R_{25}	1735.66	-2.64	1.19	1	0.69	nuv,B,V,J,H,K	18
NGC6207	late-type	0.002842	20.00	R_{25}	180.16	-1.88	1.14	1	1.33	B,V,J,H,K	18
NGC6217	late-type	0.004543	21.40	R_{25}	274.62	-2.09	1.33	1	1.40	B,V,J,H,K	18
NGC6503	late-type	0.000083	5.27	R_{25}	44.43	-2.26	0.95	1	1.70	B,V,J,H,K	18
NGC6643	late-type	0.004950	25.80	R_{25}	512.69	-1.99	1.19	1	1.55	B,V,J,H,K	18
NGC6946	late-type	0.000133	5.90	$1.5R_{25}$	678.87	-2.32	1.18	2	1.67	IRAC3.6	2
NGC7331	late-type	0.002722	14.70	$1.5R_{25}$	2715.47	-2.96	0.81	2	1.47	IRAC3.6	2
NGC7793	late-type	0.000757	3.90	$1.5R_{25}$	254.47	-3.03	0.69	2	1.09	IRAC3.6	2
IC1141	early-type	0.014670	68.00	$R_{\rm max}$[CO]($\sim$0.4R_{25})	19.26	-1.11	1.74	3,18	2.89	u,g,r,i,z,J,H,K	18
NGC2320	early-type	0.019827	83.00	$R_{\rm max}$[CO]($\sim$-0.2R_{25})	50.27	-1.11	1.90	4	3.07	J,H,K	18
NGC2768	early-type	0.004580	21.80	$R_{\rm max}$[CO]($\sim$-0.1R_{25})	1.13	-1.66	1.66	4	4.06	u,g,r,i,z,J,H,K	18
NGC3032	early-type	0.005114	25.20	$R_{\rm max}$[CO]($\sim$0.3R_{25})	5.28	-1.32	1.82	3,12	2.68	u,g,r,i,z,J,H,K	18
NGC3073	early-type	0.003853	21.10	$R_{\rm max}$[CO]($\sim$0.3R_{25})	3.70	-2.40	0.66	3,13	2.33	u,g,r,i,z,J,H,K	18
NGC3489	early-type	0.002258	11.80	$R_{\rm max}$[CO]($\sim$-0.1R_{25})	2.01	-1.86	0.97	4	3.62	u,g,r,i,z,J,H,K	18
NGC3773	early-type	0.003276	10.50	$R_{\rm max}$[CO]($\sim$0.3R_{25})	0.92	-1.24	1.17	3,14	1.91	u,g,r,i,z,J,H,K	18
NGC3870	early-type	0.002522	14.50	$R_{\rm max}$[CO]($\sim$0.4R_{25})	2.28	-1.42	1.07	3,15	2.08	u,g,r,i,z,J,H,K	18
NGC4150	early-type	0.000754	13.40	$R_{\rm max}$[CO]($\sim$-0.2R_{25})	1.13	-1.62	1.67	4	3.40	u,g,r,i,z,J,H,K	18
NGC4459	early-type	0.004036	16.10	$R_{\rm max}$[CO]($\sim$-0.1R_{25})	3.14	-1.67	1.68	4	3.79	u,g,r,i,z,J,H,K	18
NGC4477	early-type	0.004520	16.50	$R_{\rm max}$[CO]($\sim$-0.1R_{25})	0.50	-1.29	1.62	4	4.16	u,g,r,i,z,J,H,K	18
NGC4526	early-type	0.001494	16.40	$R_{\rm max}$[CO]($\sim$-0.0R_{25})	3.14	-1.16	2.19	4	3.83	u,g,r,i,z,J,H,K	18
NGC4550	early-type	0.001271	15.50	$R_{\rm max}$[CO]($\sim$-0.1R_{25})	0.50	-1.92	1.20	4	3.79	u,g,r,i,z,J,H,K	18
NGC5173	early-type	0.008069	41.20	$R_{\rm max}$[CO]($\sim$0.3R_{25})	14.12	-2.22	1.04	3,16	2.99	u,g,r,i,z,J,H,K	18
NGC524	early-type	0.007935	23.30	$R_{\rm max}$[CO]($\sim$-0.1R_{25})	3.80	-2.04	1.19	4	3.46	J,H,K	18
NGC5338	early-type	0.002722	10.30	$R_{\rm max}$[CO]($\sim$0.1R_{25})	0.44	-1.96	1.28	3,18	2.49	u,g,r,i,z,J,H,K	18
NGC5666	early-type	0.007408	35.00	$R_{\rm max}$[CO]($\sim$-0.4R_{25})	22.90	-1.08	1.34	4	2.44	u,g,r,i,z,J,H,K	18
UGC6805	early-type	0.003864	20.30	$R_{\rm max}$[CO]($\sim$0.4R_{25})	2.47	-1.82	1.02	3,18	2.31	u,g,r,i,z,J,H,K	18
UGC9562	early-type	0.004310	25.20	$R_{\rm max}$[CO]($\sim$0.4R_{25})	6.88	-2.52	0.20	3,17	1.77	u,g,r,i,z,J,H,K	18
DDO154	LSB	0.001248	4.30	$1.5R_{25}$	10.18	-3.31	1.70	2	0.09	IRAC3.6	2
HOI	LSB	0.000465	3.80	$1.5R_{25}$	22.90	-3.41	0.97	2	0.04	IRAC3.6	2
HOII	LSB	0.000474	3.40	$1.5R_{25}$	96.77	-3.30	0.94	2	0.31	IRAC3.6	2
IC2574	LSB	0.000190	4.00	$1.5R_{25}$	397.61	-3.75	0.72	2	0.10	IRAC3.6	2
LSBCF561-01	LSB	0.016034	67.00	$R_{\rm max}$[HI,UV]($\sim$1.6R_{25})	338.84	-3.39	0.75	5	0.42	u,g,r,i,z	18
LSBCF563-01	LSB	0.011681	49.00	$R_{\rm max}$[HI,UV]($\sim$3.5R_{25})	1071.52	-3.97	0.70	5	-0.21	u,g,r,i,z	18
LSBCF563-V01	LSB	0.012976	54.00	$R_{\rm max}$[HI,UV]($\sim$2.3R_{25})	186.21	-3.98	0.64	5	0.24	u,g,r,i,z	18
LSBCF564-V03	LSB	0.001612	9.00	$R_{\rm max}$[HI,UV]($\sim$3.6R_{25})	7.59	-3.97	0.45	5	0.14	u,g,r,i,z	18
LSBCF565-V02	LSB	0.012278	51.00	$R_{\rm max}$[HI,UV]($\sim$3.6R_{25})	239.88	-3.98	0.52	5	-0.14	u,g,r,i,z	18
LSBCF568-01	LSB	0.021762	91.00	$R_{\rm max}$[HI,UV]($\sim$2.0R_{25})	741.31	-3.60	0.99	5	0.27	u,g,r,i,z	18
LSBCF568-03	LSB	0.019717	83.00	$R_{\rm max}$[HI,UV]($\sim$2.1R_{25})	891.25	-3.59	0.76	5	0.41	u,g,r,i,z	18
LSBCF568-06	LSB	0.046132	205.00	$R_{\rm max}$[HI,UV]	16595.86	-3.92	0.41	5	1.14	u,g,r,i,z	18
LSBCF568-V01	LSB	0.019243	86.00	$R_{\rm max}$[HI,UV]($\sim$2.5R_{25})	794.33	-3.62	0.71	5	0.14	u,g,r,i,z	18
LSBCF574-01	LSB	0.022979	103.00	$R_{\rm max}$[HI,UV]($\sim$0.9R_{25})	758.58	-3.54	0.57	5	0.42	u,g,r,i,z	18
LSBCF574-02	LSB	0.021081	94.00	$R_{\rm max}$[HI,UV]($\sim$2.8R_{25})	380.19	-3.51	0.62	5	0.12	u,g,r,i,z	18
LSBCF577-V01	LSB	0.025978	114.00	$R_{\rm max}$[HI,UV]($\sim$1.3R_{25})	436.52	-3.18	0.50	5	0.12	u,g,r,i,z	18
LSBCF579-V01	LSB	0.020995	91.00	$R_{\rm max}$[HI,UV]($\sim$1.6R_{25})	977.24	-3.74	0.63	5	0.66	u,g,r,i,z	18
LSBCF583-01	LSB	0.007552	34.00	$R_{\rm max}$[HI,UV]($\sim$3.7R_{25})	501.19	-3.94	0.76	5	-0.57	u,g,r,i,z	18
Malin1	LSB	0.082557	380.00	$R_{\rm max}$[HI,UV]($\sim$11.3R_{25})	37153.54	-4.39	0.48	5	0.36	u,g,r,i,z,J,H,K,IRAC36	18
NGC0925	LSB	0.001845	9.20	$1.5R_{25}$	1425.31	-3.40	0.66	2	0.75	IRAC3.6	2

TABLE 1 — *Continued*

name	type	red	Dist. [Mpc]	Aperture	Area [kpc^2]	log($\Sigma_{\rm SFR}$) [M$_\odot$/yr/kpc^2]	log($\Sigma_{\rm gas}$) [M$_\odot$/pc^2]	Ref$_{\rm sfr,gas}$	log($\Sigma_{\rm star}$) [M$_\odot$/pc^2]	Band$_{\rm stellar-mass}$	Ref$_{\rm star}$
(1)	(2)	(3)	(4)	(5)	(6)	(7)	(8)	(9)	(10)	(11)	(12)
UGC5750	LSB	0.013893	60.00	$R_{\rm max}$[HI,UV]($\sim$2.0R_{25})	870.96	-3.69	0.56	5	-0.32	u,g,r,i,z	18
UGC5999	LSB	0.011314	49.00	$R_{\rm max}$[HI,UV]($\sim$1.9R_{25})	707.95	-3.57	0.80	5	-0.03	u,g,r,i,z	18
UGC6614	LSB	0.021188	92.00	$R_{\rm max}$[HI,UV]($\sim$3.1R_{25})	9120.11	-3.85	0.55	5	0.84	u,g,r,i,z,J,H,K,IRAC36	18
Arp220	z=0-LIRGs	0.018126	71.00	$R_{\rm max}$[CO]($\sim$0.1R_{25})	7.07	1.39	3.41	6	2.89	B,V,R,J,H,K	18
IRAS10190+1322	z=0-LIRGs	0.076600	340.00	$R_{\rm max}$[CO]($\sim$0.2R_{25})	45.36	0.40	2.97	7	2.91	J,H,K	18
Mrk273	z=0-LIRGs	0.037780	151.00	$R_{\rm max}$[CO]($\sim$0.2R_{25})	20.43	0.78	3.19	8	2.87	u,g,r,i,z,J,H,K	18
NGC6090	z=0-LIRGs	0.029304	123.30	$R_{\rm max}$[CO]($\sim$1.2R_{25})	268.80	-0.87	2.00	9	2.02	B,V,I,J,H,K	18
NGC6240	z=0-LIRGs	0.024480	100.90	$R_{\rm max}$[CO]($\sim$0.2R_{25})	147.41	-0.29	2.36	9	2.86	U,B,V,J,H,K	18
NGC7674	z=0-LIRGs	0.028924	115.30	$R_{\rm max}$[CO]($\sim$0.3R_{25})	118.82	-0.51	2.00	9	2.49	B,V,J,H,K	18
VV114	z=0-LIRGs	0.020067	80.00	$R_{\rm max}$[CO]($\sim$0.2R_{25})	27.34	0.24	3.23	10	2.39	Jb,J,H,K	18
BzK16000	high-z-SFG	1.52	11089	$R_{1/2}$[UV/optical, CO]	52.81	0.16	2.79	11	2.94	U,B,V,R,I,z,J,H,K	18
BzK17999	high-z-SFG	1.41	10107	$R_{1/2}$[UV/optical, CO]	40.72	0.26	2.97	11	3.15	U,B,V,R,I,z,J,H,K	18
BzK210000	high-z-SFG	1.52	11089	$R_{1/2}$[UV/optical, CO]	58.09	0.28	2.93	11	2.88	U,B,V,R,I,z,J,H,K	18
BzK4171	high-z-SFG	1.47	10640	$R_{1/2}$[UV/optical, CO]	43.01	0.08	3.03	11	3.01	U,B,V,R,I,z,J,H,K	18
EGS12007881	high-z-SFG	1.17	8024	$R_{1/2}$[UV/optical]	237.79	-0.72	2.24	11	2.09	B,R,I,Ks	18
EGS12011767	high-z-SFG	1.28	8967	$R_{1/2}$[UV/optical]	167.42	-0.85	1.89	11	2.20	B,R,I,Ks	18
EGS13003805	high-z-SFG	1.23	8536	$R_{1/2}$[UV/optical]	84.95	-0.12	3.02	11	2.94	B,R,I,Ks	18
EGS13004291	high-z-SFG	1.20	8279	$R_{1/2}$[UV/optical]	162.86	-0.28	2.93	11	2.85	B,R,I,Ks	18
EGS13004661	high-z-SFG	1.19	8194	$R_{1/2}$[UV/optical]	149.57	-0.56	1.90	11	2.26	B,R,I,Ks	18
EGS13011148	high-z-SFG	1.17	8024	$R_{1/2}$[UV/optical]	58.09	-0.45	2.41	11	2.87	B,R,I,Ks	18
EGS13011439	high-z-SFG	1.10	7434	$R_{1/2}$[UV/optical]	15.21	0.47	3.17	11	3.46	B,R,I,Ks	18
EGS13017614	high-z-SFG	1.18	8109	$R_{1/2}$[UV/optical]	124.69	-0.53	2.57	11	2.76	B,R,I,Ks	18
EGS13035123	high-z-SFG	1.12	7602	$R_{1/2}$[UV/optical]	232.35	-0.57	2.44	11	2.86	B,R,I,Ks	18
Q1623-BX599	high-z-SFG	2.33	18723	$R_{1/2}$[Hα]	24.63	0.42	3.51	11	2.64	U,G,R,J,Ks	18
Q1700-BX691	high-z-SFG	2.19	17362	$R_{1/2}$[Hα]	141.03	-0.73	2.09	11	1.97	U,G,R,J,Ks	18
Q1700-MD174	high-z-SFG	2.34	18821	$R_{1/2}$[Hα]	40.72	0.15	3.29	11	2.91	U,G,R,J,Ks	18
Q1700-MD69	high-z-SFG	2.29	18333	$R_{1/2}$[Hα]	277.59	-0.54	2.29	11	1.87	U,G,R,J,Ks	18
Q1700-MD94	high-z-SFG	2.34	18821	$R_{1/2}$[Hα]	289.53	-0.25	2.96	11	2.32	U,G,R,J,Ks	18
Q2343-BX442	high-z-SFG	2.18	17265	$R_{1/2}$[Hα]	141.03	-0.47	2.55	11	2.16	U,G,R,J,Ks	18
Q2343-BX610	high-z-SFG	2.21	17555	$R_{1/2}$[Hα]	45.36	0.36	3.40	11	2.88	U,G,R,J,Ks	18
Q2343-MD59	high-z-SFG	2.01	15634	$R_{1/2}$[Hα]	95.03	-0.68	2.68	11	1.93	U,G,R,J,Ks	18
SMMJ123549+6215	high-z-SMG	2.20	17458	$R_{1/2}$[CO]	2.54	2.25	4.65	11	4.24	U,B,V,R,I,z,J	18
SMMJ123634+6212	high-z-SMG	1.22	8450	$R_{1/2}$[CO]	52.81	0.64	3.19	11	2.78	U,B,V,R,I,z,J,K,IRAC36	18
SMMJ123707+6214	high-z-SMG	2.49	20297	$R_{1/2}$[CO]	24.63	1.01	3.34	11	3.50	U,B,V,R,I,z,J,K,IRAC36	18
SMMJ131201+4242	high-z-SMG	3.41	29645	$R_{1/2}$[CO]	28.27	1.07	3.57	11	3.06	B,R,I,z,J,K,IRAC36	18
SMMJ131232+4239	high-z-SMG	2.33	18723	$R_{1/2}$[CO]	12.57	1.31	3.80	11	3.74	B,R,I,z,J,K,IRAC36	18
SMMJ163650+4057	high-z-SMG	2.39	19311	$R_{1/2}$[CO]	18.10	1.39	4.02	11	3.65	B,V,R,I,K,IRAC36	18
SMMJ163658+4105	high-z-SMG	2.45	19902	$R_{1/2}$[CO]	2.01	2.45	4.90	11	4.61	B,R,I,K,IRAC36	18

NOTE. — Col.(1): Name. Col.(2): The galaxy type in this paper. Col.(3): The redshift. Col.(3): The distance in Mpc that is used in this work. Col.(4): The definition of the aperture used to calculate the surface density of SFR, gas and stellar mass. R_{25} means the isophotal radius at 25 mag/arcsec^{-2} (usually in B band). $R_{\rm max}$ gives the maximum extent of the galaxy at a given wavelength that is indicated in square brackets. Its value relative to R_{25} is listed in parentheses whenever possible. $R_{1/2}$ is the half light radius at a given wavelength that is indicated in square brackets. Col.(5): The de-projected area used to derive surface densities. Col.(6): The SFR surface density. Col.(7): The gas surface density. Col.(8): The references and therein for the SFR and gas surface density data. For those with two references, the first one is for H_2 and SFR data while the second is for HI data. Col.(9): The stellar mass surface density. Col.(10): The wavelength band used to measure the stellar mass. Col.(11): The references for the stellar mass data.

References: 1-Kennicutt (1998a), 2-Leroy et al. (2008), 3-Wei et al. (2010), 4-Crocker et al. (2011), 5-Wyder et al. (2009), 6-Scoville et al. (1997), 7-Graciá-Carpio et al. (2007), 8-Yun & Scoville (1995), 9-Bryant & Scoville (1999), 10-Yun et al. (1994), 11-Genzel et al. (2010), 12-Oosterloo et al. (2010), 13-Irwin et al. (1987), 14-van Driel & van Woerden (1991), 15-Sage & Welch (2006), 16-Knapp & Raimond (1984), 17-Cox et al. (2001), 18-this-work.

TABLE 2
The Parameters of Stellar Synthesis Models.

parameters	value
simple stellar populations	Chabrier (2003) IMF and Padova 1994 evolutionary tracks
metallicity	0.0004, 0.004, 0.008, 0.02 ($Z_{\odot}$), 0.05
visual extinction τ_v	[0.0, 10.0] with a step of 1
fraction of τ_V arising from the ambient ISM	0.3
fraction of ejected gas to be recycled in stars	0.0
star formation history (SFH)	exponential decline
e-folding time τ for exponential SFH	[0.03, 22.4] Gyr with a step of 0.15 in logarithm, plus 100 Gyr
galaxy age	[0.05, 12.6] Gyr with a step of 0.12 in logarithm

TABLE 3
The Sample Of Spiral Galaxies

Name	Position (J2000)	Type	Dist [Mpc]	R_{25} [arcsec]	i [o]	PA [o]
(1)	(2)	(3)	(4)	(5)	(6)	(7)
NGC0628	01 36 41.8 +15 47 00	SAc	7.30	293.17	7.00	20.00
NGC2841	09 22 02.6 +50 58 35	SAb	14.10	207.55	74.00	153.00
NGC3184	10 18 17.0 +41 25 28	SABcd	11.10	222.39	16.00	179.00
NGC3351	10 43 57.7 +11 42 14	SBb	10.10	217.33	41.00	192.00
NGC3521	11 05 48.6 -00 02 09	SABbc	10.70	249.53	73.00	340.00
NGC3627	11 20 15.0 +12 59 30	SABb	9.30	306.99	62.00	173.00
NGC4736	12 50 53.0 +41 07 13	SAab	4.70	232.87	41.00	296.00
NGC4826	12 56 43.6 +21 41 00	SAab	7.50	314.14	65.00	121.00
NGC5055	13 15 49.2 +42 01 45	SAbc	10.10	352.47	59.00	102.00
NGC5194	13 29 52.7 +47 11 43	SABbc	8.00	232.87	42.00	172.00
NGC6946	20 34 52.2 +60 09 14	SABcd	5.90	344.45	33.00	243.00
NGC7331	22 37 04.1 +34 24 57	SAb	14.70	273.60	76.00	168.00

Note. — Col.(1): Name. Col.(2): The position. Col.(3): The Hubble type. Col.(4): The distance. Col.(5): The optical size R_{25}. Col.(6): The inclination. Col.(7): The position angle.

TABLE 4
The Parameters of the Best Fit

Figures	Correlations	a	b	δ	ρ	σ
(1)	(2)	(3)	(4)	(5)	(6)	(7)
Fig. 1(a)	SFE-$\Sigma_{\rm star}$	-10.28±0.08	0.48±0.04	0.123	0.97±0.03	0.41
Fig. 1(b)	SFE-$\Sigma_{\rm gas}$	-9.85±0.08	0.35±0.04	0.092	0.97±0.03	0.49
Fig. 2(a)	$\Sigma_{\rm SFR}$-$\Sigma_{\rm star}^{0.5}\Sigma_{\rm gas}$	-4.40±0.08	1.03±0.03	0.131	1.00±0.00	0.42
Fig. 2(b)	KS Law	-3.90±0.11	1.38±0.06	0.112	1.00±0.00	0.49
Fig. 3(a)	SFE-$\Sigma_{\rm star}$ (diff. α)	-10.35±0.09	0.55±0.04	0.171	0.96±0.03	0.47
Fig. 3(b)	SFE-$\Sigma_{\rm gas}$ (diff. α)	-9.97±0.10	0.49±0.06	0.172	0.93±0.05	0.54
Fig. 3(c)	$\Sigma_{\rm SFR}$-$\Sigma_{\rm star}^{0.5}\Sigma_{\rm gas}$ (diff. α)	-4.51±0.09	1.10±0.03	0.180	0.99±0.01	0.47
Fig. 3(d)	KS Law (diff. α)	-4.17±0.14	1.65±0.09	0.125	1.00±0.00	0.55

Note. — Col.(1): The corresponding figure to a given correlation. Note that the LSB and early-type galaxies are always excluded for the KS law or the equivalent version (SFE-$\Sigma_{\rm gas}$). "diff. α" means different CO-to-H_2 conversion factors for mergers and non-mergers. Col.(2): The Y vs. X correlations. Col.(3)-Col.(5): $\log(Y) = a + b*\log(X)+\epsilon$ as given by linmix_err.pro that accounts for measured errors on both X- and Y-axis (Kelly 2007), where (a, b) are the regression coefficients and ϵ is the intrinsic random scatter about the regression and has a mean of zero and variance of δ^2. Col.(6): The linear correlation efficiency. Col.(7): The observed standard deviation of all data points from the best fit.